X-ray polarimetry as a new method of studying X-ray binary systems

Master's thesis
University of Turku
Astronomy
2025
Anastasiia Bocharova
Examiners:
Dr. Alexandra Veledina
Prof. Juri Poutanen

The originality of this thesis has been checked in accordance with the University of Turku quality assurance system using Turnitin Originality Check service.

UNIVERSITY OF TURKU
Department of Physics and Astronomy

Anastasiia Bocharova X-ray polarimetry as a new method of studying X-ray binary systems

Master's thesis, 52 pp.
Astronomy
20.05.2025

This thesis investigates black hole X-ray binaries through multi-instrument observational data, focusing on spectral and polarimetric analysis. These systems, in which a black hole accretes matter from a companion star, serve as laboratories for studying extreme astrophysical processes. The study combines data from the Imaging X-ray Polarimetry Explorer (*IXPE*) and complementary X-ray missions to analyze three black hole binaries: Cygnus X-1, Cygnus X-3, and the transient Swift J1727.8–1613.

X-ray polarimetry, enabled for the first time with imaging sensitivity by *IXPE*, has opened a new observational window into the inner regions of accreting black holes. The *IXPE* campaign on Cygnus X-1 provided the first detailed view of polarization changes across spectral states, constraining the evolving geometry of the corona. For Swift J1727.8–1613, the broadband spectrum during its hard-to-soft state transition was successfully described by a two-phase disk–corona model. In the case of Cygnus X-3, X-ray polarimetry uncovered the unique nature of its emission, shaped by complex scattering environments.

These results demonstrate how X-ray polarimetry provides direct insight into the geometry, orientation, and physical conditions of the innermost accretion flows – information previously inaccessible with traditional spectroscopy or timing alone. As a revolutionary tool in high-energy astrophysics, polarimetry significantly improves our ability to study black holes and their vicinity.

Keywords: high-energy astrophysics, X-ray binaries, polarization, spectral analysis

List of publications and contributions

The results obtained during the work on this thesis have been included in the following publications:

1. Veledina A., Poutanen J., **Bocharova A.**, et al., “Ultrasoft state of microquasar Cygnus X-3: X-ray polarimetry reveals the geometry of the astronomical puzzle”, Astronomy & Astrophysics 688, L27, 2024.

2. Kravtsov, V., **Bocharova A.**, et al., "Variability of X-ray polarization of Cyg X-1", submitted to Astronomy & Astrophysics, 2025,
   preprint: https://arxiv.org/abs/2505.03942.

3. Ahlberg, V., **Bocharova A.**, Veledina A., "The intrabinary bow shock of Cygnus X-3 unveiled by its peculiar orbital variability of X-ray polarization", preparing for submission to Astronomy & Astrophysics, 2025.

The author’s contribution includes performing orbital phase-resolved polarimetry analysis using *IXPE* data.

Contents

1 Introduction

This section provides the essential background for understanding the context and motivation of this work. A general summary of X-ray binary systems is given in Sect. 1.1, covering their classification and key observational features. Sect. 1.2 outlines black hole X-ray binaries, detailing their spectral, variability, and polarization properties. Sect. 1.3 describes the primary physical components of these systems: the accretion disk, X-ray emitting corona, and reflection features.

1.1 X-ray binary systems

An X-ray binary system (XRB) consists of a compact object – a black hole or a neutron star – and a companion star. These systems are exceptionally bright in X-rays due to the accretion of matter from the companion star onto the compact object. XRBs are typically divided into two classes based on the mass of the companion: low-mass X-ray binaries (LMXBs) and high-mass X-ray binaries (HMXBs).

In LMXBs the mass of the companion is less than one solar mass ($M_\odot$), and stable mass transfer proceeds through the inner Lagrangian point when the companion fills its Roche lobe. The configuration is shown in the top panel of Fig. 1. These sources are brighter in the X-ray band compared to the optical band, where the observed flux arises primarily from the reprocessing of X-rays in the outer parts of the accretion disk [1].

In HMXBs, the companion star does not fill its Roche lobe and instead loses mass through a stellar wind. For this system to be bright in X-rays, the companion star must be massive (more than $10M_\odot$) to produce a strong wind. As a result, the optical luminosity of the companion dominates the total emission of the system [1]. The configuration is shown in the bottom panel of Fig. 1.

The difference between these two configurations leads to distinct lifetimes for each class. In LMXBs, the lifetime is determined by the timescale of mass transfer,

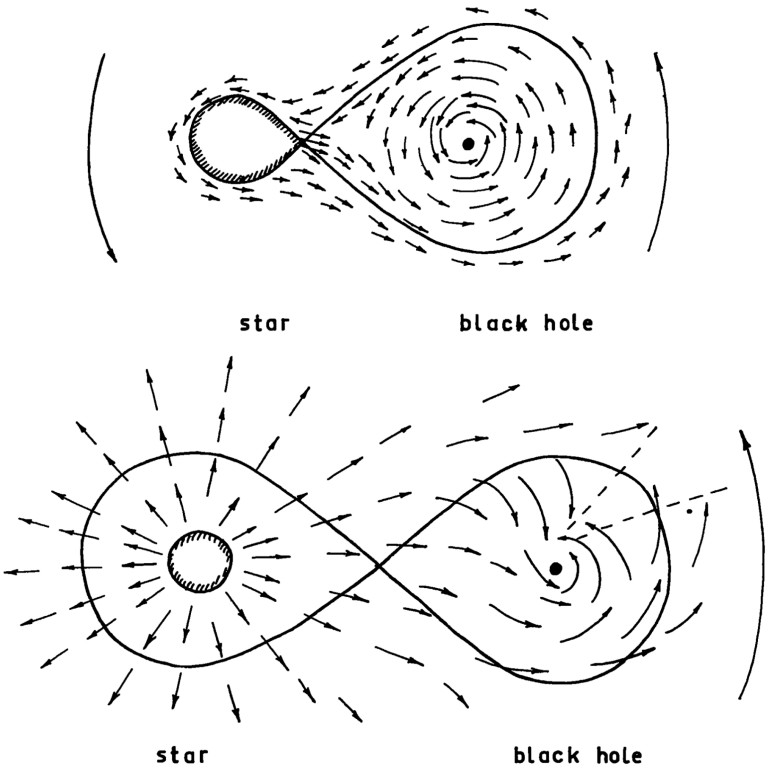

Figure 1. Two regimes of matter loss in X-ray binaries. *Top*: the companion fills its Roche lobe and the mass transfer proceeds through the inner Lagrangian point. *Bottom*: the companion's size is less than its Roche lobe, the outflow is through the stellar wind. The figure is from [2].

which typically ranges from $\sim 10^7$ to 10^9 years. In contrast, the lifetime of HMXBs is set by the evolution of the massive companion star, resulting in shorter lifetimes on the order of $\sim 10^5$ to 10^7 years. This difference in lifetime also shapes the spatial distribution of these systems within the Galaxy: HMXBs tend to lie close to the Galactic plane, as expected for young systems, whereas LMXBs are commonly found near the Galactic center and in globular clusters. These distributions are shown in Fig. 2.

Current catalogs list several hundred X-ray binary (XRB) systems in our Galaxy, making them relatively rare among the vast population of stellar systems [4, 5]. Such rarity is consistent with the very specific conditions and improbable evolutionary steps required for these systems to form. The processes that lead to the formation of bright X-ray sources with accreting compact objects are still poorly understood.

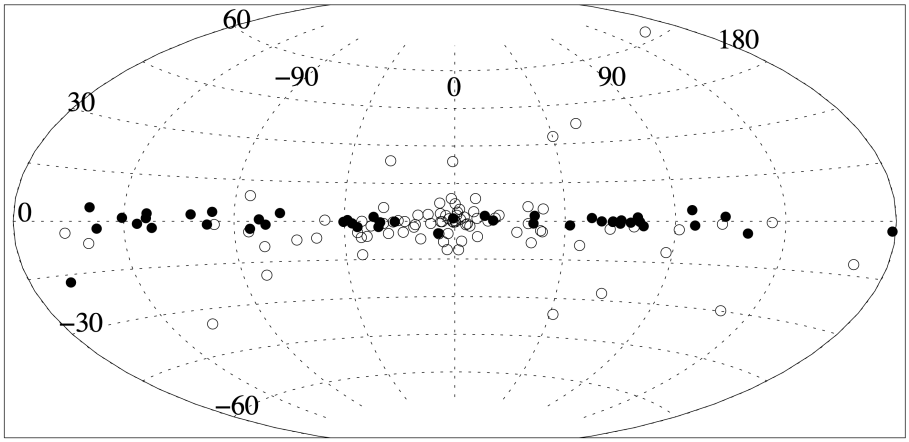

Figure 2. Distribution of LMXBs (open symbols) and HMXBs (filled symbols) in galactic coordinates from [3].

However, the advent of a new generation of instruments may bring us closer to solving these puzzles.

1.2 Observed properties of Black Hole X-ray binaries

The study of X-ray binaries relies on a combination of observational techniques that investigate different physical aspects of these systems. Spectral analysis provides information about the energy distribution of emitted radiation and enables the identification and modeling of primary emission components such as thermal emission from the accretion disk, Comptonized emission from the corona, and reflection features. Through spectral fitting, it is possible to constrain parameters such as the disk temperature, optical depth, and the structure and composition of the emitting regions.

Timing analysis, which focuses on the variability of the source flux across a wide range of timescales, offers additional insights into the dynamical behavior of the accretion process. Features such as flares, dips, quasi-periodic oscillations, and spectral transitions can be linked to instabilities or structural changes in the accretion disk or corona.

A more recent addition to this observational framework is X-ray polarimetry,

which measures the polarization properties of X-ray photons. Polarimetric data provide a direct probe of the geometry and physical conditions in the innermost regions of the system, particularly where scattering and magnetic fields dominate the radiative processes. When used in combination with spectral and timing techniques, X-ray polarimetry offers a powerful diagnostic tool, capable of resolving uncertainties in existing models and addressing long-standing questions about the emission mechanisms in black hole X-ray binaries.

1.2.1 Spectra

Black hole binaries (BHB) are observed in two spectral states, which are believed to correspond to different configurations of the accretion process [6]. As shown in Fig. 3, the spectral profile of the most famous XRB – Cygnus X-1 (Cyg X-1) – changes dramatically. The "soft" (or "high") state is characterized by a dominant soft component below 10 keV and a complex non-thermal emission tail extending beyond 500 keV [7]. The soft component is interpreted as thermal emission from an optically thick geometrically thin disk around a black hole, and can be described by a multicolor disk model (for example, `DISKBB`, as in [8, 9]), which approximates the spectrum from the Shakura-Sunyaev [2] blackbody disk. However, the high-energy tail emission is not part of standard disk models. To describe it, more complex models must be applied – for example, the hybrid Comptonization model (details in Sect.1.3.2, [10]).

Another observed spectral state – the "hard" (or "low") state – differs significantly from the soft state. In this case, the energy flux peaks at approximately 100 keV, rather than showing a prominent low-temperature disk component. The spectra can generally be described by thermal Comptonization models, with electron temperatures in the range of $kT_e = 75 - 110$ keV, as observed, for example, in Cyg X-1 [11].

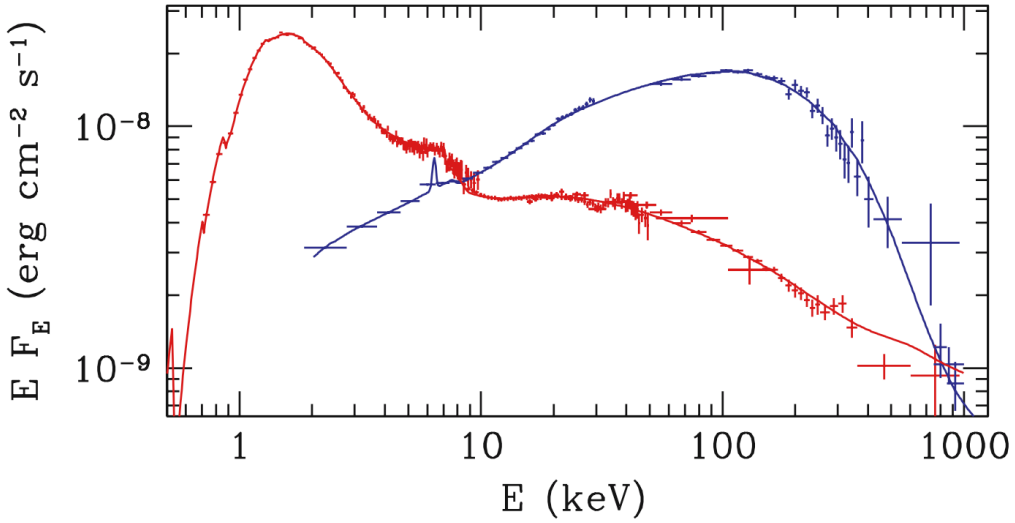

Figure 3. Energy spectrum of Cyg X-1 in the hard (*blue*) and soft (*red*) states. The figure is from [6].

Two types of spectra (hard and soft) can be explained by two distinct stable accretion flow regimes: a hot, optically thin, geometrically thick flow that exists only at low luminosities and a cool, optically thick, geometrically thin disk. These regimes are unified in the truncated disk model [6, 12], illustrated in Fig. 4. At low accretion rates, the inner accretion disk is believed to be truncated at a large radius and replaced by a hot, optically thin, geometrically thick flow. This hot inner flow efficiently upscatters a small number of seed photons, producing a hard thermal Comptonization spectrum ($N(E) \propto E^{-\Gamma}$) with a photon index $\Gamma \sim 1.5$–1.8 and a high-energy cutoff around ~ 100 keV. The high ratio of power in the electrons to that in the seed photons illuminating them ($\mathcal{L}_h/\mathcal{L}_s \gg 1$) leads to inefficient Compton cooling and a correspondingly high electron temperature. As the accretion rate increases, the cool, optically thick disk gradually extends inward, providing more seed photons and cooling the hot electrons more efficiently, which results in the soft spectrum.

At higher accretion rates, a spectral transition occurs, leading to the soft state, where the accretion disk extends down to the innermost stable circular orbit (ISCO)

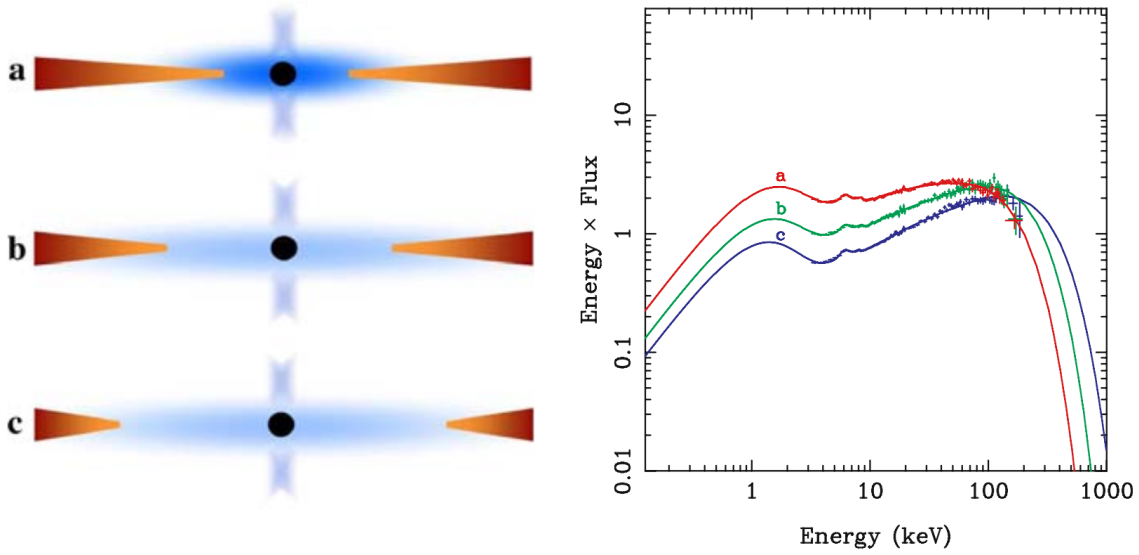

Figure 4. Range of low/hard state geometries in the truncated disk model (*right panel*), together with their predicted spectra (*left panel*). When the disk is truncated far from the black hole, few disk photons are intercepted by the hot flow, resulting in a hard Comptonized spectrum, with large fraction of disk photons observed directly. As the disk extends further under the hot flow, more disk photons are intercepted, softening the spectrum due to cooler electron temperatures, despite the disk being hotter and less distinct. The figure and description are from [6].

and dominates the X-ray emission. In this case, the ratio $\mathcal{L}_h/\mathcal{L}_s \sim 1$, resulting in strong cooling and possibly non-thermal Comptonization, which produces a weak, steep power-law tail with a photon index $\Gamma \gtrsim 2$ [13, 14]. These transitions are often asymmetric: the system typically reverts to the hard state at a lower luminosity, due to changes in the disk structure [15].

Although the truncated disk model explains many observed features, alternative scenarios offer additional insights. These include jet-dominated models, which propose that the base of the jet contributes significantly to the observed hard X-ray emission [16, 17]; magnetically supported disk models, which suggest that strong magnetic fields can stabilize the inner flow and influence its emission properties [18]; and disk-corona interaction models, where a compact corona above the disk significantly affects the Comptonized emission [13, 19]. The variety of models highlights the complexity of accretion physics and underscores the need for continued

observational and theoretical studies.

1.2.2 X-ray variability

X-ray binaries show both long- and short-term variability, reflecting complex physical processes that drive accretion onto compact objects. Short-term variability, which occurs on timescales from milliseconds to seconds, includes stochastic noise and quasi-periodic oscillations (QPOs). QPOs have been studied extensively since their discovery over thirty years ago and have been widely used to map the characteristics of the accretion flow [20, 21]. In the Fourier domain, quasi-periodic oscillations (QPOs) appear as narrow peaks in the power density spectrum (PDS), which is obtained by performing a Fourier transform of the source light curve and calculating the squared amplitude as a function of frequency. QPOs are typically divided into two types: low-frequency (LF), with centroid frequency below 30 Hz, and high-frequency (HF), with centroid frequency above 60 Hz [22]. LF QPOs are commonly observed in black hole systems, whereas HF QPOs are rare and weaker in amplitude.

Long-term variability occurs on timescales from days to months and is associated with global changes in the accretion disk. This includes state transitions, disk instabilities, and variations in the mass accretion rate. Many LMXBs are transients that exhibit episodic outbursts separated by periods of quiescence. As the system evolves through an outburst, it typically transitions between distinct spectral states: hard, soft, and intermediate, each characterized by unique spectral and timing properties [23, 24].

These transitions are often tracked using diagnostic tools such as the hardness intensity diagram (HID), the hardness-rms diagram (HRD) and the rms-intensity diagram (RID), as shown in Fig. 5 for the transient GX 339–4 BHB [25]. Here, rms refers to the root-mean-square amplitude of flux variability in a given Fourier

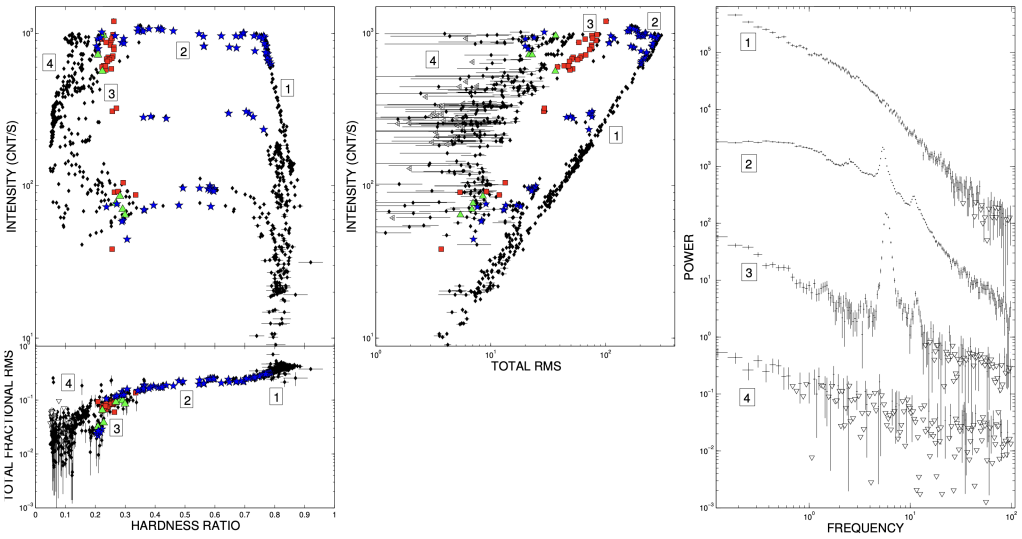

Figure 5. *Top-left panel*: HID for outbursts of a Galactic XRB GX 339–4. *Bottom left panel:* the corresponding rms-hardness diagram. *Middle panel*: RID for these outbursts. *Right panel*: power density spectra for the same outbursts. The figure is from [25].

frequency range, typically expressed as a fraction of the total flux. It quantifies the strength of short-term (aperiodic or quasi-periodic) variability and is particularly useful for distinguishing between different spectral states. For instance, variability is typically low (below 5%) in the soft state and high (above 30%) in the hard state. Long-term monitoring has revealed hysteresis in the state transitions: the path traced through the HID differs between the rise and decay of an outburst, suggesting state-dependent changes in disk geometry and inner flow properties [15]. In HID shown in the top-left panel of Fig. 5, four branches can be identified: right and left branches correspond to the hard and soft states, respectively. The other two sides represent more complex intermediate states.

QPO properties also evolve across spectral states. In the HRD, a tight correlation between spectral hardness and rms amplitude is often observed, while the RID traces how variability evolves with source flux. In particular, a linear relation between rms and flux – the so-called "hard line" – is characteristic of the hard state and reflects intrinsic fluctuations in the mass accretion rate [26]. These diagrams serve

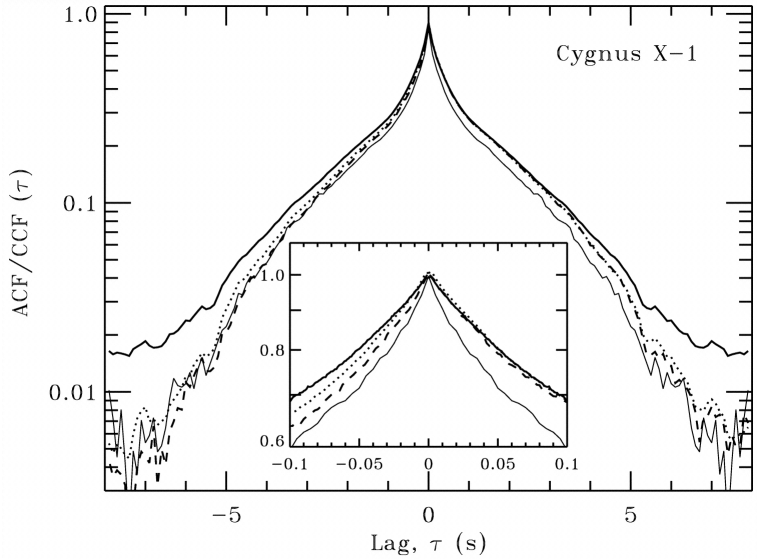

Figure 6. Auto- and cross-correlation functions of Cyg X-1 observed in 1997 December. *Solid curves* show the ACFs for the 2–5 keV energy band (*thick curves*) and the 24–40 keV band (*thin curves*). *Dotted curves* show the CCF between the 8–13 keV band and the 2–5 keV band, and *dashed curves* represent the CCF for the 24–40 keV band vs. the 2–5 keV band. The figure and description are from [27]

as powerful classification tools, as they are sensitive to changes in accretion geometry and emission processes [25].

Another way to explore the relationship between soft and hard X-ray bands is through autocorrelation functions (ACF), which are obtained by applying an inverse Fourier transform to the PDS, and cross-correlation functions (CCF), which measure the correlation between two light curves at different energy bands as a function of time lag. An example is shown in Fig. 6 for Cyg X-1, where an asymmetry in the CCF is apparent. This asymmetry arises from a delay of the hard X-rays relative to the soft X-rays [27, 28]. These time lags provide valuable information about the spatial and physical structure of the inner accretion flow [29]. The frequency dependence of these lags helps to constrain the geometry and timescales of radiative processes occurring near the compact object [30, 31].

Together, the timing properties and the long-term evolution of X-ray binaries across multiple outbursts serve as powerful diagnostics of the accretion flow geometry

and spectral state. They offer crucial insights into the physical mechanisms driving accretion onto compact objects [32].

1.2.3 Polarization

Polarimetry is another powerful technique for studying compact objects. Measuring the linear polarization of X-rays from cosmic sources provides valuable insights into the geometry of the system's inner regions. The first detection of X-ray polarization from a cosmic source was made by the *OSO*-8 satellite in the 1970s. More recently, missions such as *INTEGRAL* (operated in the 0.1–10 MeV range) and *Astrosat* (working in the 100–300 keV range) conducted polarization measurements at higher energies. Currently, the only mission dedicated to polarimetry in the soft X-ray band (2–8 keV) is *IXPE* (details in Sect. 2.3).

Polarized emission propagating along the z-axis can be described using the Stokes parameters [33]:

$$I = \langle E_x^2 + E_y^2 \rangle,$$
$$Q = \langle E_x^2 - E_y^2 \rangle,$$
$$U = \langle 2E_x E_y \cos\delta \rangle,$$
$$V = \langle 2E_x E_y \sin\delta \rangle,$$

where E_x, E_y are the projections of the electric vector, which is proportional to the instantaneous electric field along the x-axis (y-axis), and δ is the phase lag of E_y behind E_x. For 100% polarized emission $I_{\rm pol}$, the following equation holds $I_{\rm pol} = \sqrt{Q^2 + U^2 + V^2}$. In practice, most observed emission is only partially polarized. Therefore, it is useful to define a polarization degree P, which represents the fraction of polarized radiation in the total observed emission: $P = I_{\rm pol}/I$. Furthermore, the circular polarization component is often negligible, allowing us to assume $V = 0$.

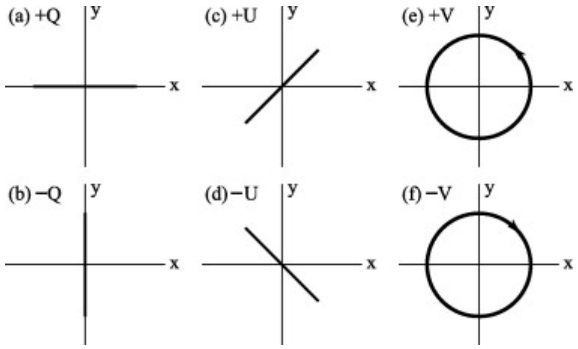

Figure 7. Polarization for different values of the Stokes parameters.
(a) $Q > 0,\ U = 0,\ V = 0$; (b) $Q < 0,\ U = 0,\ V = 0$; (c) $U > 0,\ Q = 0,\ V = 0$; (d) $U < 0,\ Q = 0,\ V = 0$; (e) $V > 0,\ U = 0,\ Q = 0$; (f) $V < 0,\ U = 0,\ Q = 0$.
The figure is from [34].

Under this assumption, the system of equations simplifies to:

$$P = \frac{\sqrt{Q^2 + U^2}}{I}$$

$$Q = IP\cos 2\phi$$

$$U = IP\sin 2\phi$$

Here, ϕ is the angle between the x-axis and the electric field direction, or the polarization angle (PA), and P is the linear polarization degree (PD).

Several high-energy processes naturally generate polarized X-ray emission. One of the most common mechanisms is synchrotron radiation, produced when relativistic charged particles gyrate in magnetic fields. In this case, the polarization vector is perpendicular to the magnetic field lines [35]. This mechanism is frequently encountered in pulsar wind nebulae, supernova remnants, and relativistic jets from active galactic nuclei [36–38].

In extreme magnetic fields, such as those near magnetars, quantum electrodynamics predicts the occurrence of vacuum polarization [39]. In this phenomenon, different photon polarization modes propagate at different phase velocities through magnetized vacuum. This results in a rotation or modulation of the polarization angle and potentially leads to a high polarization fraction in thermal surface emission [40].

Another important mechanism is Thomson and Compton scattering: initially unpolarized photons that scatter at non-zero angles acquire a significant polarization fraction. This is especially relevant in systems with complex geometries, such as X-ray binaries and accreting black holes, where photons from the accretion disk scatter off electrons in the surrounding material [41, 42]. The resulting polarization depends on the system's viewing angle and the geometry of the scattering region.

X-ray polarimetric observations with *IXPE* have already provided critical insights into the structure and dynamics of black hole X-ray binaries [43, 44]. These results demonstrate the diagnostic power of X-ray polarimetry in probing the geometry, emission mechanisms, and magnetic environments of accreting systems.

1.3 Main spectral components

The X-ray spectra of black hole X-ray binaries can be decomposed into several components, each corresponding to specific regions and physical processes within the system. Generally, three components can be distinguished: thermal emission from the accretion disk, Comptonized emission from the corona, and reflection from the disk. These components not only shape the spectral energy distribution but also contain information about the geometry and physical processes occurring in the innermost regions of the system.

The accretion disk is typically modeled as geometrically thin and optically thick, emitting as a multi-temperature blackbody that peaks in the soft X-ray band [2]. It is believed to extend close to the innermost stable circular orbit in the soft state, while in the hard state it may be truncated at a larger radius [28]. The difference in geometry between the hard and soft states is shown in Fig. 8. However, this is only one of the possible scenarios for spectral transitions (see Sect. 1.3.1). Above or within this disk lies the corona, a region of hot, optically thin electrons that Compton upscatter seed photons from the disk, producing a hard X-ray power-law

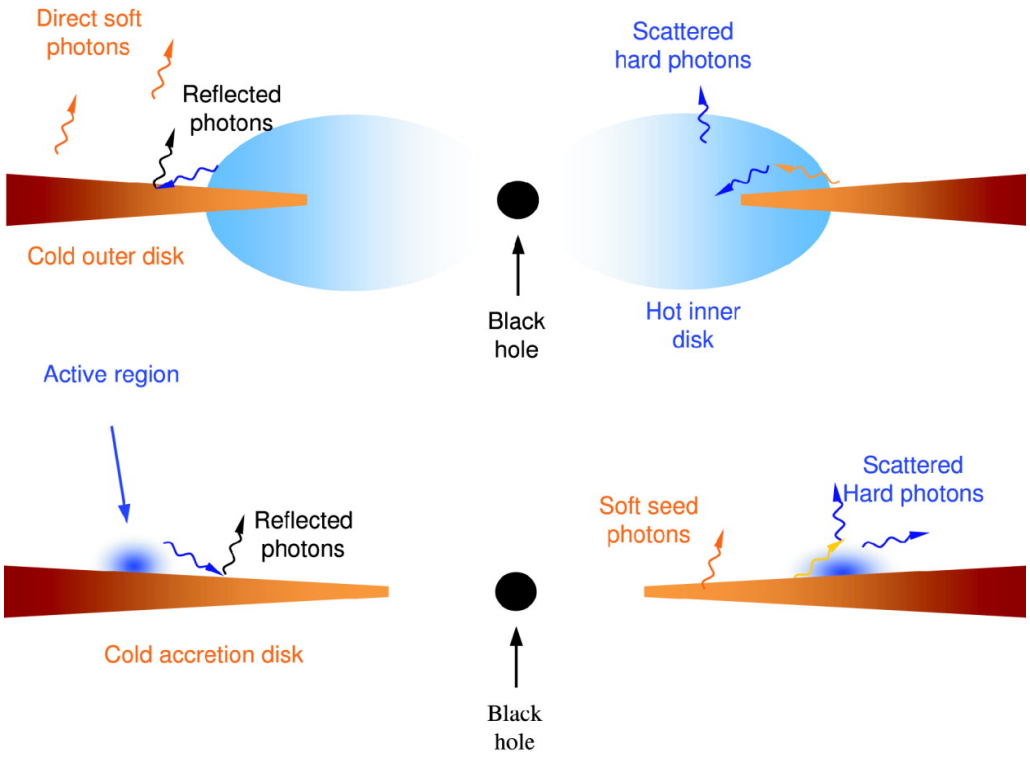

Figure 8. A schematic representation of the geometry of XRBs in the hard (*top panel*) and soft (*bottom panel*) states. In the hard state, hot inner accretion flow surrounded by optically thick cold accretion disk. In the soft state, active regions are above the optically thick accretion disk extending close to ISCO. The figure is from [12].

continuum [45]. The exact geometry of the corona is still debated. The details are described in Sect. 1.3.2. A fraction of coronal emission is intercepted and reflected by the disk, producing a continuum characterized by fluorescent lines and a broad Compton hump [46] (see Sect. 1.3.3). The shape and strength of these features depend on the ionization state, inclination, and inner radius of the disk, as well as the height and geometry of the illuminating source.

Understanding the interaction and geometry of these components is essential for interpreting spectral state transitions. Accurate modeling of all components is crucial for tracing changes in accretion flow structure across different spectral states.

1.3.1 Accretion Disk

Astrophysical black holes can be characterized using only two parameters: mass and spin. Ideally, steady accretion flows should be determined using only these parameters combined with the mass accretion rate. Observational characteristics of these systems should be affected by just two additional parameters: the angle of inclination and any dynamic effects arising from variable behavior. The mass (M) and the orbital inclination (i) are directly observable from the binary orbit [47], yet determining the spin and accretion rate ($\dot{M}$) is not trivial. The luminosity generated per unit mass accreted is regulated by the efficiency of gravitational energy release, which depends on the gravitational potential at the ISCO. For a non-rotating (Schwarzschild) black hole, the ISCO lies at $r = 6R_{\rm g}$ ($R_{\rm g} = GM/c^2$ is the gravitational radius, where G is the gravitational constant, M is the black hole mass, and c is the speed of light), resulting in an accretion efficiency of $\eta \sim 0.057$, whereas for a maximally rotating (Kerr) black hole, the ISCO can shift to $r = R_{\rm g}$, increasing efficiency to $\eta \sim 0.42$ [48]. The total accretion luminosity is usually approximated as $L_{\rm acc} \approx \eta \dot{M} c^2$, where η depends on the spin and the disk structure.

In addition to the uncertainty about total energy of the system, there is greater uncertainty in determining the fraction of energy that is radiated versus what drives the winds, jets or is carried along with the material [6]. The observed X-ray luminosity only partially represents the total mass accretion rate. Moreover, pressure or magnetic forces in a hot and/or magnetically dominated flow can complicate the theoretical description of the system even further [49].

A fundamental constraint on the energy output of accreting systems is set by the Eddington luminosity. It corresponds to the point at which the radiation pressure balances the gravitational force. For spherical symmetry and fully ionized hydrogen, the Eddington luminosity is given by $L_{\rm Edd} = \frac{4\pi G M m_p c}{\sigma_T} \approx 1.3 \times 10^{38} \left(\frac{M}{M_\odot}\right)$ erg s^{-1}, where m_p is the proton mass and σ_T is the Thomson cross-section. The Eddington

limit serves as an upper bound on the steady luminosity produced by accretion unless outflows or relativistic beaming are present.

The accretion flow structure is established by balancing gravitational heating and radiative cooling. In the classic Shakura-Sunyaev disk [2] model, it is assumed that the gravitational potential energy released through viscous dissipation is entirely converted into local thermal emission. This model neglects advection of heat, outflows, and energy losses through winds or jets, and assumes that energy is radiated efficiently at each radius.

The basic assumption in Shakura-Sunyaev disk is that shear stresses $t_{r\phi}$ are proportional to total pressure $P_{\rm total} = P_{\rm gas}+P_{\rm radiation}$, such that $t_{r\phi} = \alpha P_{\rm total}$, the disk at a specific radius $r = R/R_{\rm g}$ emits as a blackbody of temperature $T(r) \propto r^{-3/4}$. The solution gives a geometrically thin disk, except for luminosities near Eddington. At high luminosities approaching or exceeding the Eddington limit, radiation pressure dominates and the disk may become geometrically thicker. It requires modifications to the standard model or transitions to alternative accretion regimes.

The model described above may effectively describe steady accretion flows, but it encounters serious limitations when applied to systems with low mass accretion rates and temperatures in the range of hydrogen ionization 10^4–10^5 K. Under these conditions, the Shakura-Sunyaev disk becomes both thermally and viscously unstable. When the disk material is mostly neutral, its opacity is relatively low, allowing thermal energy to escape efficiently. However, a slight increase in temperature can abruptly increase the opacity, trapping thermal energy within the disk and causing a thermal runaway until hydrogen is fully ionized. As a result, viscous stresses increase with the corresponding rise in pressure, leading to a temporary increase in the mass accretion rate.

This process is self-limiting. As the material in the disk is exhausted, the pressure and temperature are reduced, which eventually leads to hydrogen recombination.

When the temperature drops below the critical ionization threshold, the cycle resets, ready to repeat with the next temperature fluctuation [50]. This hydrogen ionization instability, known as the "limit cycle", originates locally at specific radii but can perturb neighboring regions through sudden changes in mass accretion rate. The contrast in behavior between ionized and neutral regions can lead to structural disruption of the global disk, gradually converting it into a quiescent state where neutral hydrogen dominates.

In this context, the disk no longer follows the classic Shakura–Sunyaev model with a constant accretion rate across all radii. Instead, during quiescence, the disk maintains a relatively uniform temperature but exhibits a strongly radially dependent accretion rate that decreases toward the inner regions. The disk instability model (DIM) provides an explanation for this behavior. According to the DIM [51], during quiescence the disk slowly accumulates mass from the companion star. When the temperature exceeds the hydrogen ionization threshold, the instability is triggered. A heating wave then propagates rapidly through the disk, initiating an outburst. However, since only a fraction of the disk material is accreted during this phase, the outer regions eventually cool, a cooling wave travels inward, and the system returns to quiescence, completing the cycle.

At very high mass accretion rates, another fundamental limitation of the Shakura–Sunyaev model arises in the inner disk regions, where radiation pressure begins to dominate over gas pressure. In this regime, the disk becomes thermally and viscously unstable: small increases in temperature lead to increased radiation pressure, which enhances viscous heating and further raises the temperature, resulting in runaway heating. However, when radial advection of energy is taken into account, this additional cooling mechanism can stabilize the flow [49]. The instability may remain localized to the radiation pressure-dominated regions and does not necessarily disrupt the entire disk. In this context, the standard α-prescription fails to accurately

describe disk behavior [6].

This picture becomes more complex in the context of X-ray binaries, where the effect of irradiation cannot be neglected. As noted in [6], irradiation from the central X-ray source plays a crucial role in maintaining high temperatures across the disk, even at large radii. This external heating can suppress hydrogen recombination, allowing accretion to proceed at rates exceeding those supplied by the companion star. Consequently, the disk is gradually exhausted, leading to a decrease in both temperature and mass accretion rate, which in turn reduces the irradiation. Once the outer disk regions cool below the hydrogen ionization temperature, the cycle is restarted. The observed optical brightness of X-ray binary disks typically exceeds the predictions of the standard Shakura-Sunyaev model, further underscoring the significance of irradiation.

Despite progress in theoretical modeling, the shapes of observed light curves of many transient and persistent X-ray binaries remain puzzling. In particular, neutron star and black hole binaries with long orbital periods show complex outburst patterns. These may arise from a combination of thermal-viscous instabilities, irradiation, tidal forces, or increased mass transfer from an irradiated companion. However, the general agreement between disk instability models and long-term light curve behavior across a broad range of systems suggests that a modified version of the Shakura-Sunyaev disk still provides a robust model for interpreting accretion in X-ray binaries [6, 51].

1.3.2 X-ray corona

Specta of XRBs often show high-energy tails and rapid variability that cannot be explained by thermal emission from the accretion disk alone. These features are well-explained by introducing a hot, optically thin plasma – the corona – which Compton upscatters soft photons from the disk. The presence of reflection signatures

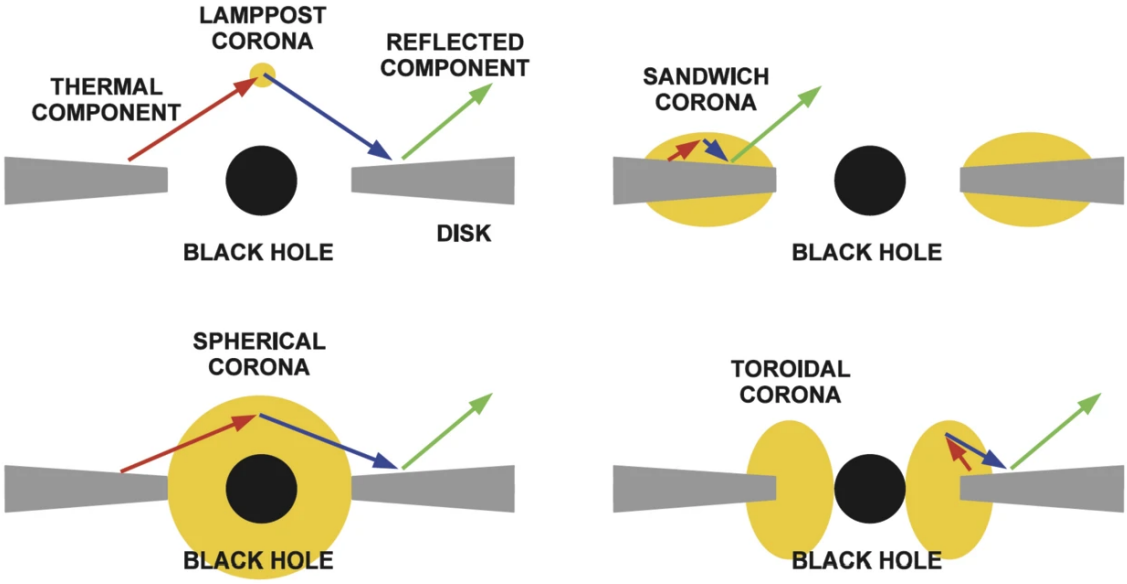

Figure 9. Possible corona geometries from [57].

and spectral transitions further supports a coronal component in emission models of XRBs.

The term "corona" was first implemented to describe energetic plasma surrounding the black hole, by analogy with the solar corona [52]. Geometries possibly formed by corona are illustrated in Fig. 1.3.2. In the "lamp-post" model, the corona is a compact source on the rotation axis of the black hole [53]. This geometry is often used to model relativistically broadened reflection spectra in active galactic nuclei (AGN) and XRBs [54, 55]. In the “sandwich” model, the corona is the atmosphere above the inner parts of the accretion disk. This configuration is particularly invoked to explain Comptonized spectra in the soft state of black hole binaries [7, 13, 19]. The coronal geometry can vary over time, and this phenomenon was observed in BHB [56].

Electrons in the corona may exhibit purely thermal distributions or include a

high-energy non-thermal tail. These electrons Compton upscatter soft photons originating either from the blackbody emission of the accretion disk or from synchrotron radiation emitted by the electrons themselves. The latter is efficient when a non-thermal tail extends beyond the thermal distribution [28]. Such non-thermal tails have been observed in the soft state of black hole binaries, reaching MeV energies [7]. In contrast, the majority of the X-ray spectra observed in the hard state can be explained by thermal electron Comptonization, although a weak non-thermal tail might persist, or most Comptonization could arise from the bulk motion of plasmoids within the accretion flow [58].

The two-phase disk–corona model (hybrid Comptonization model), introduced in [19, 59] and further developed in [13], was proposed to explain the high-energy tails, observed in the soft state of many BH XRBs. In this model, the accretion disk consists of two components: a cool, optically thick disk and a hot, optically thin corona. The soft photons from the accretion disk are Compton upscattered in the corona. Some of these hard X-rays irradiate the disk, heating it and generating more soft photons, which again feed the corona. This cycle creates an energy balance and results in a combined spectrum featuring both soft thermal emission and a high-energy non-thermal tail.

Modeling the corona in XRBs is essential for interpreting their high-energy emission. It provides constraints on the temperature, optical depth, and geometry of the hot plasma responsible for Comptonization. These properties, in turn, affect both the observed continuum and the reflection features. Understanding the coronal structure is crucial for explaining spectral state transitions and the connection between accretion and jet formation.

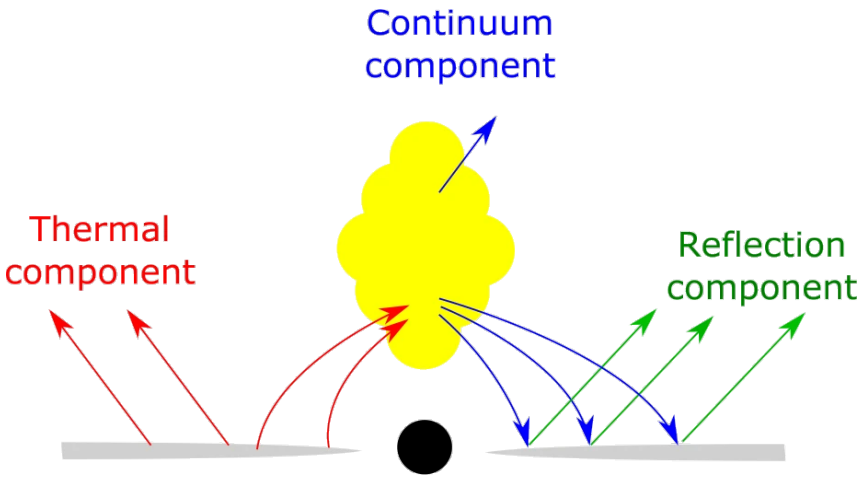

Figure 10. Cartoon of the disk-corona model from [62].

1.3.3 Reflection

Relativistic reflection signatures are frequently detected in the X-ray spectra of accreting black holes, including BHBs, and are thought to arise from illumination of the accretion disk by a hot corona. The process is illustrated in Fig. 10. In the Figure, a black hole (black circle) accretes from an optically thick, geometrically thin disk (gray layers). The disk emission can be described as a multi-temperature blackbody, since the gas is assumed to be close to local thermal equilibrium. Photons from the blackbody disk undergo inverse Compton scattering by free electrons in the corona (yellow cloud in Fig. 10). The Comptonized photons produce a power-law spectrum with an exponential high-energy cutoff (continuum component in Fig. 10). Compton scattering and absorption followed by re-emission give rise to a reflection component [60, 61].

Reflection is energy-dependent: at low energies, the reflection probability decreases due to photoelectric absorption, while at high energies, Compton downscattering and reduced scattering cross-section reduce the number of reflected photons. Key features in the X-ray reflection spectrum include fluorescent emission lines

below 10 keV, the Fe K-edge within 7–10 keV, and the Compton hump at 20–30 keV, as shown in Fig.11. The Fe Kα complex is the strongest fluorescent emission line, located at 6.4 keV for neutral or weakly ionized iron, shifting up to 6.97 keV for H-like Fe ions. The Compton hump arises from photoelectric absorption of low-energy photons combined with multiple electron down-scattering of high-energy photons. The overall reflection spectrum of the accretion disk, as observed far from the source, includes emission from all points of the disk and relativistic effects – Doppler boosting, gravitational redshift, light bending, and black hole photon capture – occurring in the strong gravity region around the black hole [46]. Consequently, spectral features appear broadened and skewed to a distant observer, as depicted in Fig. 11.

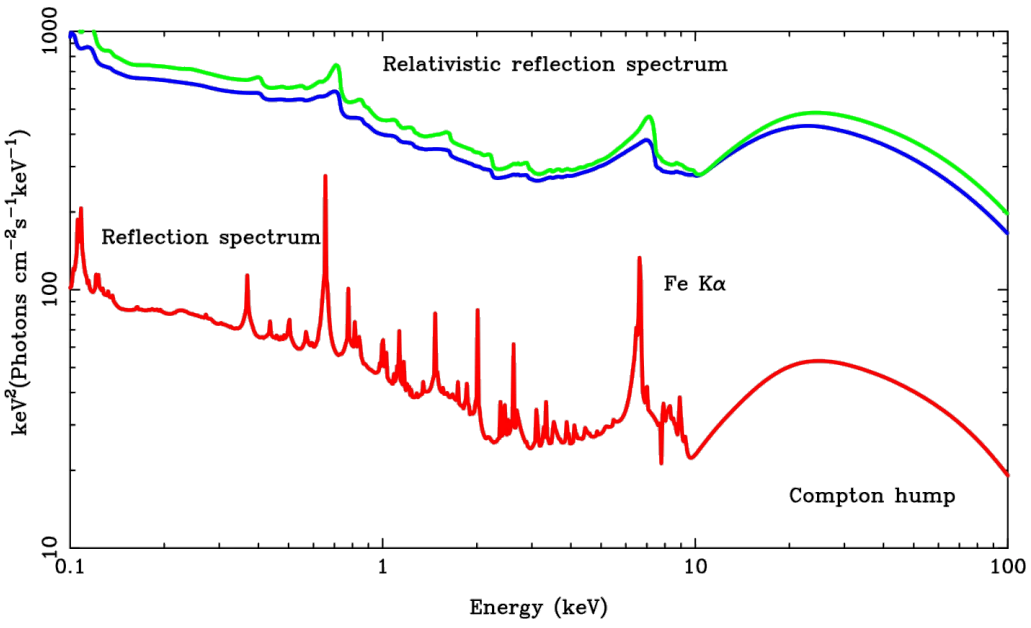

Figure 11. Reflection spectrum in the rest-frame of the gas in the disk (red curve) and relativistic reflection spectra of the whole disk as seen by a distant observer (green and blue curves) from [62].

Since the reflection spectrum originates from the innermost region of the accretion disk, analyzing reflection features in X-ray spectra of accreting black holes is a

powerful tool for studying their immediate surroundings. This approach allows us to probe the inner structure of accretion disks and the properties of nearby material, such as the corona. Furthermore, modeling these features enables measurements of black hole spin and offers tests of fundamental physics in strong gravity environments [62, 63].

1.3.4 Open questions

Despite decades of observational and theoretical efforts, the physical structure and emission mechanisms in BH XRBs remain active areas of investigation. One of the main challenges lies in the degeneracy of spectral models: different geometrical configurations can produce similar spectral features, making it difficult to determine the actual structure of accretion environment. This uncertainty also affects the interpretation of spectral state transitions, where spectral changes may originate from variations in the inner radius of the accretion disk, changes in the corona or the jet contribution. Timing analysis combined with spectral modeling offers additional constraints. However, even this approach often fails to uniquely determine the system's geometry and the physical processes near the compact object.

X-ray polarimetry has emerged as a powerful tool to address these problems. Unlike spectroscopy and timing analysis alone, polarimetry is directly sensitive to the geometry and orientation of emitting regions. This sensitivity enables independent constraints on the structure of the corona, the inclination of the disk, and the nature of scattering and reflection processes. With the launch of dedicated polarimetric missions like *IXPE*, it is now possible to combine spectral, timing, and polarimetric data to build a more complete and physically consistent picture of accreting black holes.

2 Observational data

The Earth's atmosphere is opaque to X-rays, so X-ray astronomy could not begin until the late 1950s, when suitable spacecraft were developed. The first instruments to detect X-rays from the Sun were flown on balloons and small Aerobee rockets with simple Geiger counters. The discovery of the first celestial X-ray source, Sco X-1 [64], was made by an Aerobee rocket in 1962. Later, in 1975, the map of cosmic X-ray sources was expanded via a number of transatlantic balloon missions. A major breakthrough came with the launch of the *Uhuru* satellite, which operated from 1970 to 1973 and carried two large-area proportional counters; it completed the first X-ray all-sky survey with a sensitivity down to 0.5 mCrab [65]. The development of X-ray focusing optics, such as Wolter mirrors, subsequently enabled imaging capabilities. Launched in 1978, *Einstein* was the first mission to observe extended X-ray sources.

Alongside these instruments, the Orbiting Solar Observatory 8 (*OSO-8*), launched in 1975, was the first mission to successfully measure X-ray polarization from a celestial source – the Crab Nebula – using Bragg crystal polarimeters [36]. Later, the Compton Gamma Ray Observatory (*CGRO*, operational from 1991 to 2000) included instruments with limited but pioneering sensitivity to gamma-ray polarization.

The 1990s saw the launch of many outstanding X-ray astronomy missions. Among the early ones were *Granat*, the Roentgen Satellite (*ROSAT*), and the Advanced Satellite for Cosmology and Astrophysics (*ASCA*). These were followed in the mid-1990s by *BeppoSAX* and the Rossi X-ray Timing Explorer (*RXTE*). Later, the Chandra X-ray Observatory and *XMM-Newton* were launched – both of which remain operational to this day. This era is often regarded as the beginning of the so-called golden age of X-ray astronomy [66].

Currently, several satellite missions are dedicated to X-ray observations. In this study, we utilize data from the spectrometers onboard *NuSTAR* and *INTEGRAL*, as well as from the Imaging X-ray Polarimetry Explorer (*IXPE*) – the first mission fully

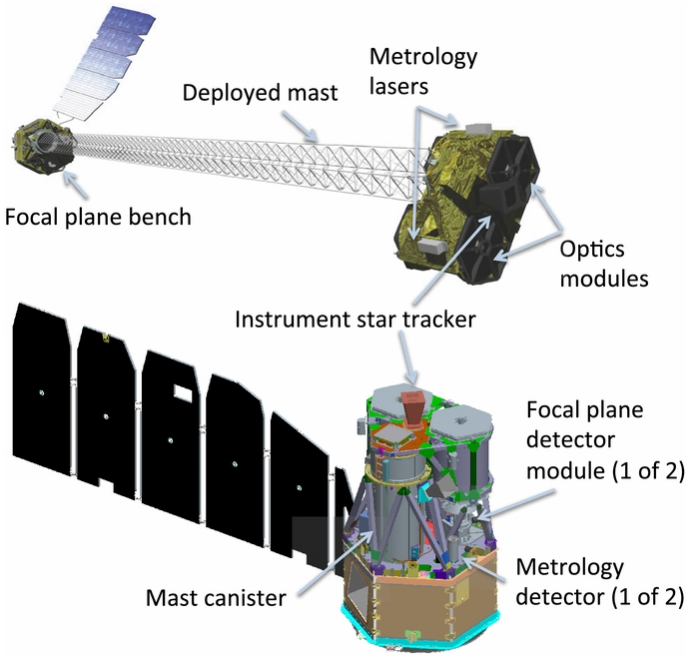

Figure 12. Diagram of *NuSTAR* observatory in the stowed (bottom) and deployed (top) configurations from [67].

dedicated to X-ray polarimetry. This section outlines the main detection principles of these instruments.

2.1 The Nuclear Spectroscopic Telescope Array

The Nuclear Spectroscopic Telescope Array (*NuSTAR*) was launched on 13 June 2012 [67]. It operates in the hard X-ray band, covering energies from 3 to 79 keV. The observatory consists of two co-aligned telescopes mounted on a three-axis stabilized spacecraft, allowing precise pointing at selected targets. The illustration of the observatory is presented in Fig. 12.

The *NuSTAR* observatory consists of two nearly identical X-ray optical systems and focal plane detectors, separated by a mast approximately 10 meters in length, designed to enhance sensitivity through combined imaging. The instrument employs an aspect and metrology system, including a star tracker and laser units, to monitor and correct for misalignments caused by mast deformations. These measurements

are incorporated during data processing to accurately project individual X-rays onto the sky, ensuring precise alignment and focus, as well as the correct generation of instrument response files [67].

The *NuSTAR* observatory achieves an angular resolution of 18″ full width at half-maximum (FWHM), with a half-power diameter of 58″. Its energy resolution is approximately 0.4 keV at 10 keV and 0.9 keV at 60 keV. The typical observing efficiency is 55% for sources within the declination range $55° > \delta > -55°$, increasing to nearly 90% for sources at high latitudes.

Typical *NuSTAR* targets include accreting neutron stars and black holes, AGNs, XRBs, supernova remnants, and galaxy clusters. Exposure times range from 20 ks for bright sources to 500 ks for faint sources. The main advantages of *NuSTAR* are its high sensitivity in the hard X-ray band and simultaneous broadband spectral coverage, making it ideal for studying the spectral properties of XRBs, including reflection features.

2.2 International Gamma-Ray Astrophysics Laboratory

The *INTEGRAL* (International Gamma-Ray Astrophysics Laboratory) mission, operated by the European Space Agency (ESA), was launched on 17 October 2002 [68]. It is dedicated to high-resolution gamma-ray astronomy, combining fine spectroscopy and imaging to investigate some of the most energetic phenomena in the universe. *INTEGRAL* provides a spectral resolution of approximately 2.5 keV at 1 MeV and an angular resolution of 12′ (FWHM). The spacecraft carries four instruments (the payload is shown in Fig. 13):

- IBIS (Imager on Board the *INTEGRAL* Satellite) is a coded-mask gamma-ray imager that covers the 15 keV to 10 MeV energy range [69].
- SPI (SPectrometer on *INTEGRAL*) is a high-resolution gamma-ray spectrometer operating from 20 keV to 8 MeV [70].

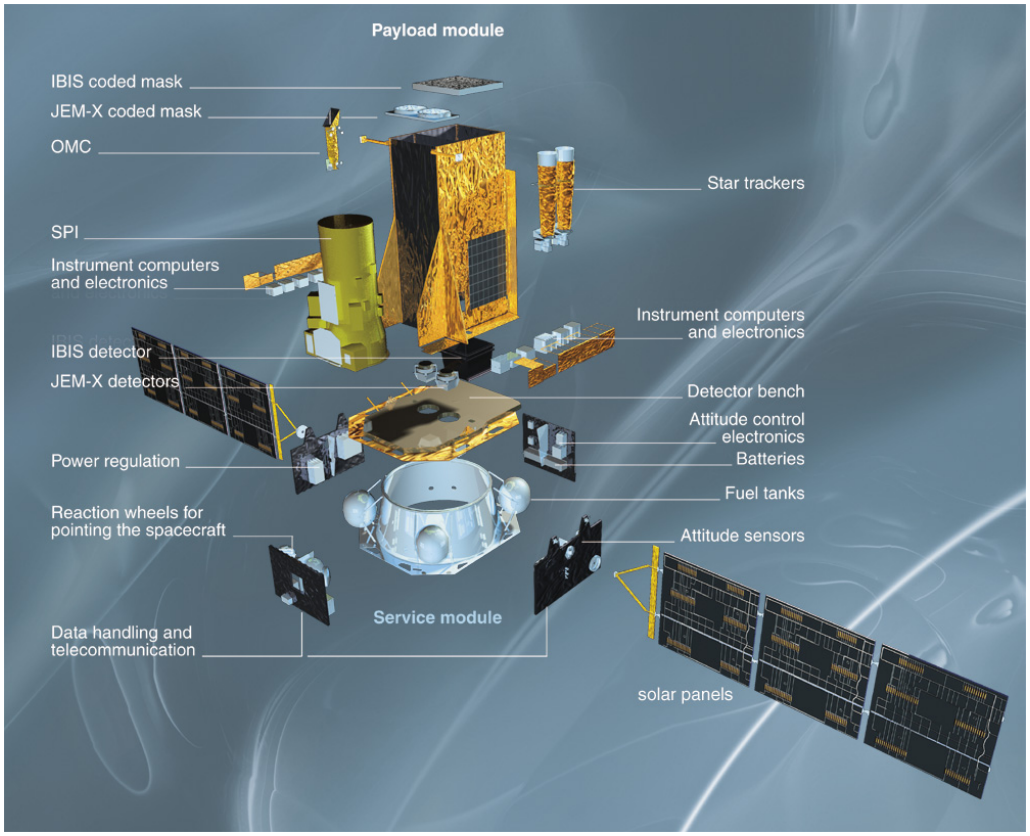

Figure 13. *INTEGRAL* instruments, credit: European Space Agency.

- JEM-X (Joint European X-ray Monitor) complements the gamma-ray instruments by observing in the 3 to 35 keV range [71].
- OMC (Optical Monitoring Camera) observes in the Johnson V-band [72].

In this study, data from *INTEGRAL*, particularly from the IBIS instrument, are used to constrain the high-energy tail of the broadband spectrum at energies beyond 80 keV.

2.3 Imaging X-ray Polarimetry Explorer

IXPE was launched on 9 December 2021 into a 600 km-altitude equatorial orbit [73]. The payload, illustrated in the top panel of Fig. 14, consists of three identical X-ray telescopes. Each telescope comprises a mirror module assembly (MMA) paired with a polarization-sensitive detector unit (DU) at its focal point. Data from the DUs

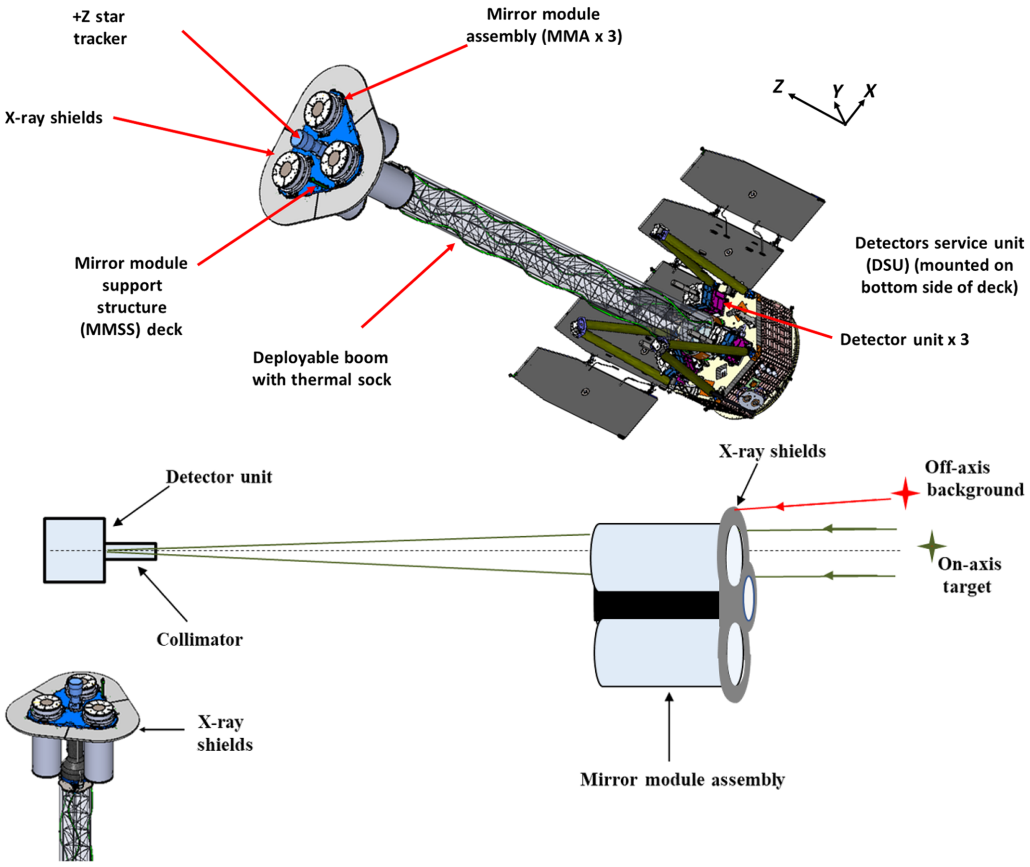

Figure 14. *Top panel:* the *IXPE* Observatory highlighting the key scientific payload elements. *Bottom panel:* the combination of the forward x-ray shields and the collimator mounted to each detector. The image is from [73].

are processed by the detector service unit (DSU) and transmitted to the ground via the spacecraft computer. X-ray shields combined with collimators (see the bottom panel of Fig. 14) ensure that only X-ray photons passing through the MMAs reach the DUs, effectively blocking background radiation.

Each MMA consists of 24 concentrically nested mirror shells, closely packed with approximately 2 mm separation, each shell being 600 mm in length. The mirror shells are made of nickel/cobalt alloy, which provides optimal reflectivity over the *IXPE* energy band of 2 to 8 keV. The MMA is also covered by a pair of thermal shields designed to minimize heat loss while remaining transparent to X-rays. The telescope's field of view (FOV) is limited by the detector size of $12.9' \times 12.9'$ (corresponding to the full detector area of 15×15 mm). The instrument's response is energy-dependent and decreases toward the edges of the FOV: at low energies, it retains 73% of its on-axis value, whereas at 8 keV it drops to 40% of the on-axis value.

The DUs, positioned in the focus of each MMA, measure the position, energy, and arrival time of X-ray photons, as well as their polarization. The core component of the DU is the gas pixel detector (GPD), which captures the ionization tracks of photoelectrons generated by X-ray photons interacting with a gas medium (dimethyl ether). The polarization of the incoming radiation is determined by the initial direction of the emitted photoelectron, while the photon's energy and position are determined by the total collected charge and the location of the initial interaction, respectively. The schematic in Fig. 15 illustrates the incident X-ray entering through the beryllium window and interacting with the gas, producing a photoelectron. This photoelectron creates an ionization trail that drifts through a gas electron multiplier, amplifying the signal before it is registered by a pixel anode readout.

The *IXPE* ground system consists of multiple components designed to support mission operations and data transmission. A primary ground center is located in

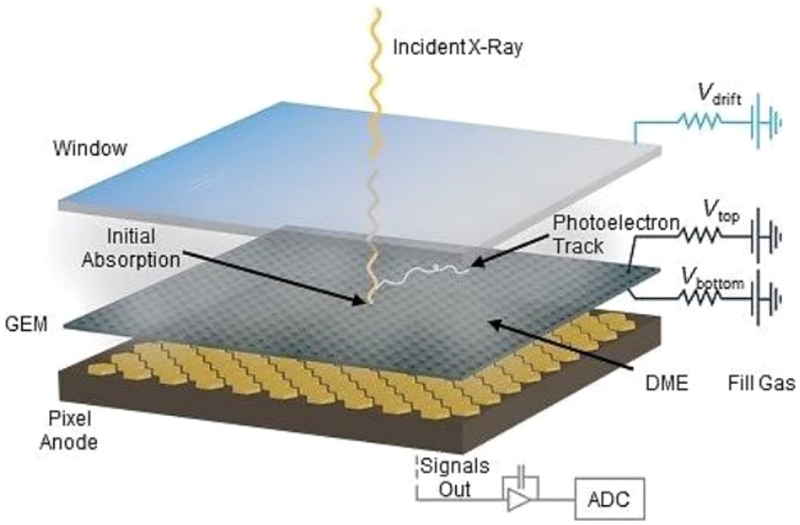

Figure 15. Schematic of the GPD from [73].

Malindi, Kenya, and a backup station is located in Singapore, to ensure continuous communication coverage. Missions are operated from the mission operation center (MOC). The Science Operations Center (SOC) is responsible for the observing plan that is sent to the MOC for execution. The SOC receives observing data that are processed and calibrated there to produce science data products. These data are publicly available through NASA's High Energy Astrophysics Science Archive Research Center (HEASARC).

2.4 Methods and data analysis

In X-ray astronomy, transforming raw detector output into scientifically interpretable results involves a structured multi-step process. The first step is data reduction, which includes corrections for instrumental effects such as charge transfer inefficiency, gain shifts, bad pixels, photon pileup, and detector dead time [74]. These corrections are applied using the calibration databases developed by the respective instrument teams. In this work, the HEASARC's calibration database (CalDB) was used. After calibration, the recorded events are filtered based on energy range, timing, and spatial criteria, followed by background subtraction. However, since the

sources analyzed in this study were sufficiently bright, background subtraction was omitted.

Spectral analysis proceeds by constructing an energy spectrum from the detected events. Accurate spectral fitting requires two key instrument response files: the response matrix file (RMF), which stores information of the energy redistribution properties of the detector, and the ancillary response file (ARF), which describes the effective area as a function of energy. To reconstruct the incident spectrum of the source, forward-fitting techniques are applied: physical emission models are convolved with the instrumental response and then compared to the observed data. Model parameters are optimized using statistical methods, typically χ^2-minimization for high-count data or maximum likelihood for low-count data [75]. In this work, spectral analysis and fitting is performed using the XSPEC package [76], version 12.14.1, and χ^2 statistics was chosen based on the high count rate.

Before the launch of *IXPE*, X-ray polarimeters relied on Compton scattering to measure polarization (for example, *INTEGRAL* and *Astrosat*), which had limited sensitivity and required higher photon energies. *IXPE* polarization detectors utilize the photoelectric effect (see Sect. 2.3), representing a significant technological breakthrough. In such detectors, the direction of the emitted photoelectron is correlated with the polarization vector of the incoming photon, enabling precise reconstruction of the polarization angle. The azimuthal direction of the photoelectron emitted after absorption of an incident photon is correlated with the electric vector of the incoming radiation. The resulting distribution of azimuthal angles follows a $\cos^2\phi$ modulation, where ϕ is the true polarization angle, from which the polarization degree and angle can be derived [77]. This method is most effective at lower X-ray energies, allowing for much greater sensitivity to polarization at 2–8 keV.

IXPE polarimetric analysis involved constructing modulation curves which represent the distribution of detected events as a function of the photoelectron emission

azimuthal angle. The polarization degree is determined by fitting this distribution with a sinusoidal function, accounting for the instrument's modulation factor – a measure of its response to 100% polarized light. To ensure unbiased results, it is essential to correct for systematic effects, instrumental asymmetries, and any contribution from background polarization [78]. For this purpose, instrument response files are applied. In this work, we used response files from CalDB version 13 for *IXPE*.

IXPE observational data are publicly available at HEASARC[1]. Data reduction and analysis are performed using the IXPEOBSSIM package [79]; in this work, version 31.0.1 was used. Data can be filtered in time, energies, or region using the `xpselect` tool. The `xpselect` tool allows for filtering data by time, energy, or spatial region. The package also supports phase-resolved analysis: the `xpphase` tool calculates the phase of each event based on a user-defined period and zero point. Binned products, such as polarization properties in defined energy bins, can be generated using the `xpbin` tool. Additionally, unbinned spectra of the Stokes parameters can be extracted for spectral analysis.

[1] https://heasarc.gsfc.nasa.gov/cgi-bin/W3Browse/w3browse.pl

3 Main results

This section presents results obtained from the analysis of observational data collected by X-ray telescopes. Three distinct objects were studied: the first discovered XRB Cygnus X-1, the unique ultraluminous XRB Cygnus X-3, and the black hole transient Swift J1727.8–1613. Sect. 3.1 summarizes the main findings from the 2.5-year *IXPE* observational campaign on Cyg X-1. Section 3.2 presents the results of an orbital phase-resolved polarimetric analysis of Cygnus X-3. The result of broad-band spectral modeling of Swift J1727.8–1613, based on a hybrid Comptonization model, is provided in Sect. 3.3.

3.1 Cygnus X-1

Cygnus X-1 is a bright and persistent X-ray binary system, discovered in 1964 [80]. It consists of a stellar-mass black hole of 21.2 ± 2.2 $M_\odot$ in orbit around an OB supergiant star, with an orbital period of 5.6 days. The system is located at a distance of $2.22^{+0.18}_{-0.17}$ kpc [81]. Reflection modeling indicates that the black hole is rapidly spinning, with a spin parameter $\alpha > 0.92$ [82]. Cyg X-1 also produces two radio-emitting jets [83] and is therefore classified as a microquasar. Due to its brightness and persistence, it became the first target for polarization studies of BHB.

Theoretical predictions of the Cyg X-1 polarization degree suggested a value around 1% [42], based on an inclination angle (the angle between the black hole spin axis and the line of sight) of $i = 27.5^\circ \pm 0.8^\circ$, derived from optical observations [81]. The first polarization measurements, performed with the *OSO-8* space telescope, yielded a PD of $2.44 \pm 1.07\%$ and a PA of $-18^\circ \pm 13^\circ$ at 2.6 keV [84], though these were considered upper limits due to instrumental limitations.

At higher energies, *INTEGRAL* detected strong polarization ($\sim 67\% \pm 30\%$) in the 0.4–2 MeV band, consistent with synchrotron emission from a jet. In contrast,

Table 1. *IXPE* observing log and measured X-ray polarization of Cyg X-1.

Epoch	Obs. ID		Date	Hardness	State	PD, %	PA, deg
1	01002901	2022	May 15	0.569	H	4.0 ± 0.2	-21 ± 2
2	01250101		June 18	0.610	H	3.9 ± 0.3	-26 ± 3
3	02008201	2023	May 2	0.280	S	2.5 ± 0.4	-17 ± 5
4	02008301		May 9	0.271	S	2.4 ± 0.3	-23 ± 4
5	02008401		May 24	0.151	S	2.1 ± 0.3	-25 ± 4
6	02008501		June 13	0.210	S	1.5 ± 0.3	-26 ± 6
7	02008601		June 20	0.240	S	2.1 ± 0.2	-36 ± 3
8	03002201	2024	April 12	0.610	H	3.9 ± 0.5	-25 ± 4
9	03003101		May 6	0.589	H	3.1 ± 0.5	-28 ± 5
10	03010001		May 26	0.620	H	4.6 ± 0.5	-28 ± 3
11	03010101		June 14	0.649	H	4.6 ± 0.6	-33 ± 3
12	03002599[a]		October 10	0.389	S	2.8 ± 0.3	-18 ± 3
13	03002599[a]		December 12	0.280	S	2.8 ± 0.2	-25 ± 3

[a]Observations 12 and 13 were conducted as parts of one observation with ID 03002599, which was then manually split in two parts.

lower energy observations (250–400 keV) showed weak polarization (below 20%), supporting a thermal Comptonization in a corona [85]. Observations by *PoGO+* in the 19–181 keV range placed an upper limit on PD at 8.6%, suggesting an extended corona geometry [86].

The *IXPE* observational campaign on Cyg X-1 included 13 observations throughout 2.5 years. The first observation, carried out in May 2022, reported a PD of $4.01 \pm 0.20\%$ and a PA of $-20.7^\circ \pm 1.4^\circ$ [43]. The analysis revealed that the bright X-ray emitting plasma is extended in a direction perpendicular to the radio jet. The relatively high polarization degree may suggest a more edge-on viewing angle than

previously inferred from optical data, or it could point to additional, as yet unidentified, physical mechanisms contributing to X-ray emission in black hole systems [43].

In this study, we performed polarization analysis of all 13 *IXPE* observations, utilizing the most recent available *IXPE* response files. The polarization properties derived from each of these observations are summarized in Tab. 1. To characterize the spectral state of the source, we computed the hardness ratio, defined as the ratio of *IXPE* photon flux in the 4–8 keV band to that in the 2–4 keV band. A hardness ratio below 0.5 indicates a soft spectral state, whereas values above 0.5 correspond to a hard state.

Fig. 16 shows the spectral and polarimetric measurements obtained by *IXPE* across all observational epochs. The data reveal a clear distinction between the emission properties in the soft and hard spectral states. Specifically, the PD in the hard state is approximately twice as high as in the soft state (around 4% versus 2%, respectively). In contrast, the PA demonstrates no obvious dependence on the spectral state, varying between $-36°$ and $-17°$ across all observations. The polarization spectra, shown in Fig. 17, further support these trends: PD increases with energy in both spectral states and remains consistently higher in the hard state, while PA remains constant with energy and independent of spectral state.

The analysis of the 2.5-year *IXPE* observational campaign demonstrates that Cyg X-1 exhibits a stable polarization degree during the hard state, with a noticeable drop in polarization degree observed in the soft state. In contrast, the polarization angle remains mostly unaffected by the spectral state.

Polarized X-ray emission from regions near the black hole provides crucial information about the geometry of the emitting plasma. Continued polarimetric monitoring across different spectral states allows us to track changes in polarization degree and angle, providing constraints on the geometry and physical conditions

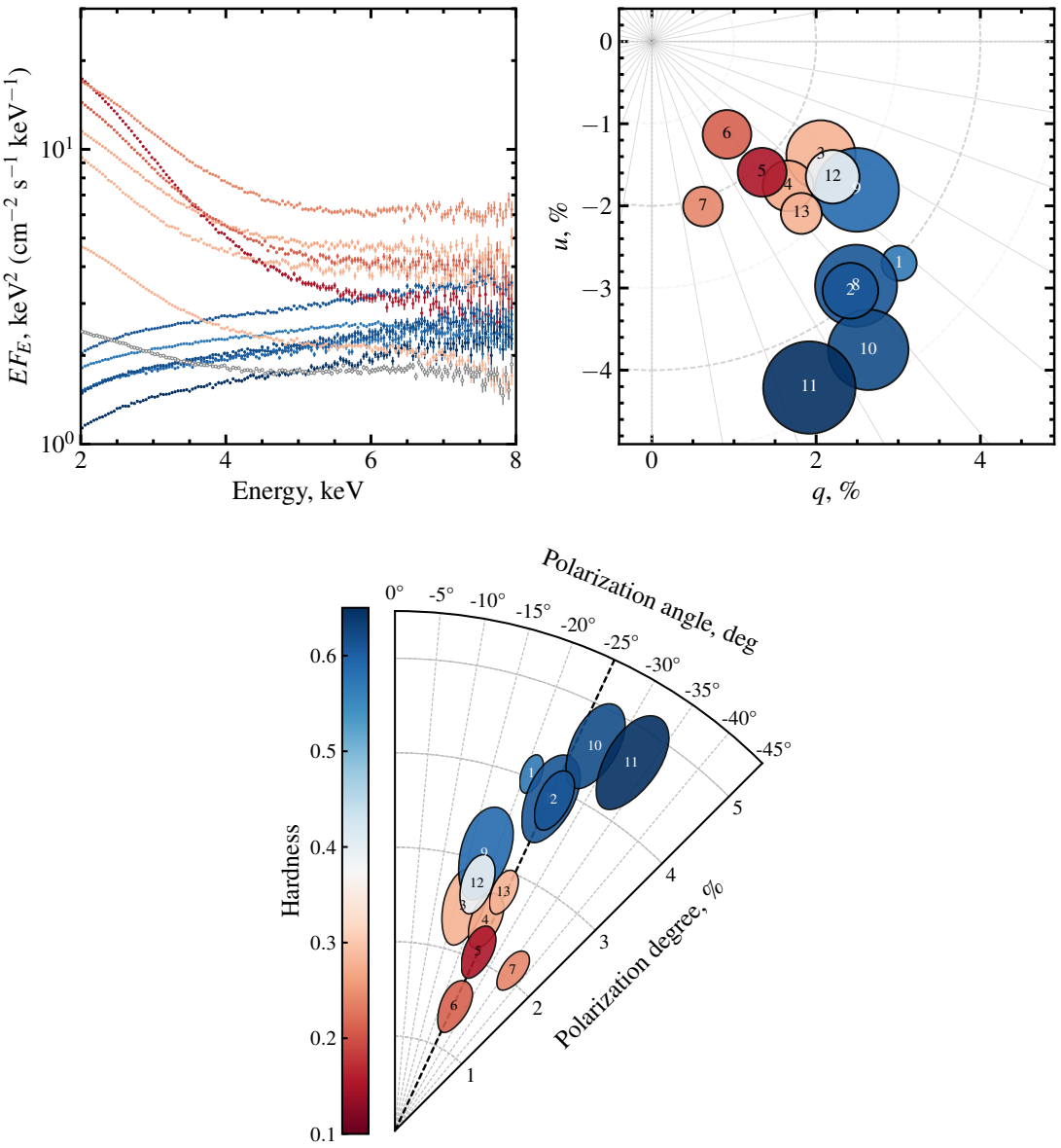

Figure 16. Spectral and polarization properties of Cyg X-1 for each observation with hardness shown in color. The black dashed line shows the direction of the radio jet. The figure is created by the author of the thesis and used in [87].

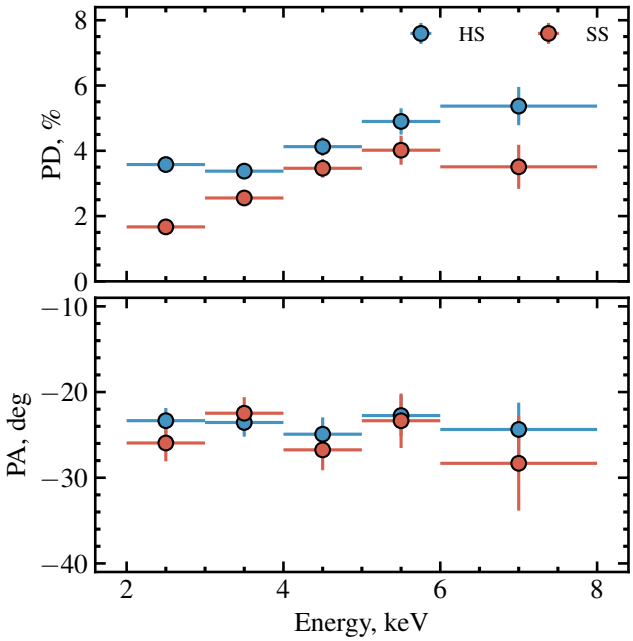

Figure 17. Polarization spectrum of Cyg X-1 averaged across hard and soft state observations. The figure is created by the author of the thesis.

of the accretion environment. In particular, combining polarization measurements with known orbital and superorbital variability enables the separation of emission components originating in distinct regions. Full orbital coverage in polarization is especially informative, as it reveals how the observed polarization properties change with viewing angle, offering deeper insights into the structure and orientation of the system [87].

3.2 Cygnus X-3

Cygnus X-3 (Cyg X-3) is one of the first X-ray sources discovered [88] and one of the brightest in the radio band [89]. Moreover, it is the only known XRB in our Galaxy that has a Wolf-Rayet star as a companion and is one of the few Galactic binaries with detectable γ-ray emission [90]. Cyg X-3 is located in the Galactic plane at a distance of 9.67 ± 0.5 kpc [91], and due to the high absorption along the line of sight, the optical counterpart is not visible. The orbital period is very short

for an XRB – 4.8 hours [16] – and is known to change rapidly over time [92]. An orbital inclination of $i = 29.5° \pm 1.2°$ was obtained from photometric variations in X-rays and infrared [93]. Cyg X-3 switches between several X-ray spectral states, which are linked to its radio properties [94] (see the left panel in Fig. 18). The

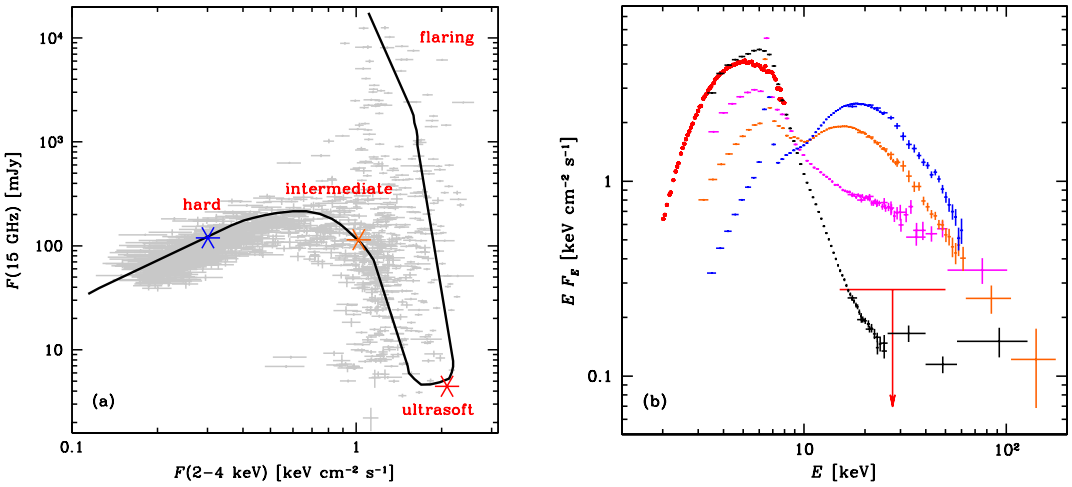

Figure 18. *Left panel*: Radio-X-ray track made by Cyg X-3 across different spectral states (data are from [95]). *Right panel*: a set of average broadband spectra corresponding to the hard (blue), intermediate (orange), ultrasoft (black), and soft non-thermal (magenta) states, as introduced in [94]. *IXPE* data are shown with red symbols and the 2σ upper limit at 30 keV (in red) is from Swift/BAT. The figure is from [96].

highest observed radio fluxes are reached when the object transits from an ultrasoft state to the so-called flaring state, where the hard X-ray flux drops dramatically, resulting in a blackbody-dominated spectrum that peaks at a few keV and exhibits a high-energy tail (see the right panel in Fig. 18).

IXPE first observed Cyg X-3 in the hard state in October-November 2022 (the "Main" observation), and later that year the object started a transition toward the soft state, so a new observation was organized in December 2022 (the "ToO" observation). In June 2024, *IXPE* observed the source in the ultrasoft state. The results of these observations are shown in Fig. 19 [44, 96].

In the hard state, a very high degree of polarization was detected: PD $= 20.8 \pm$ 0.3% in the 2–8 keV range, and the polarization angle of PA $= 90.2° \pm 0.5°$ was

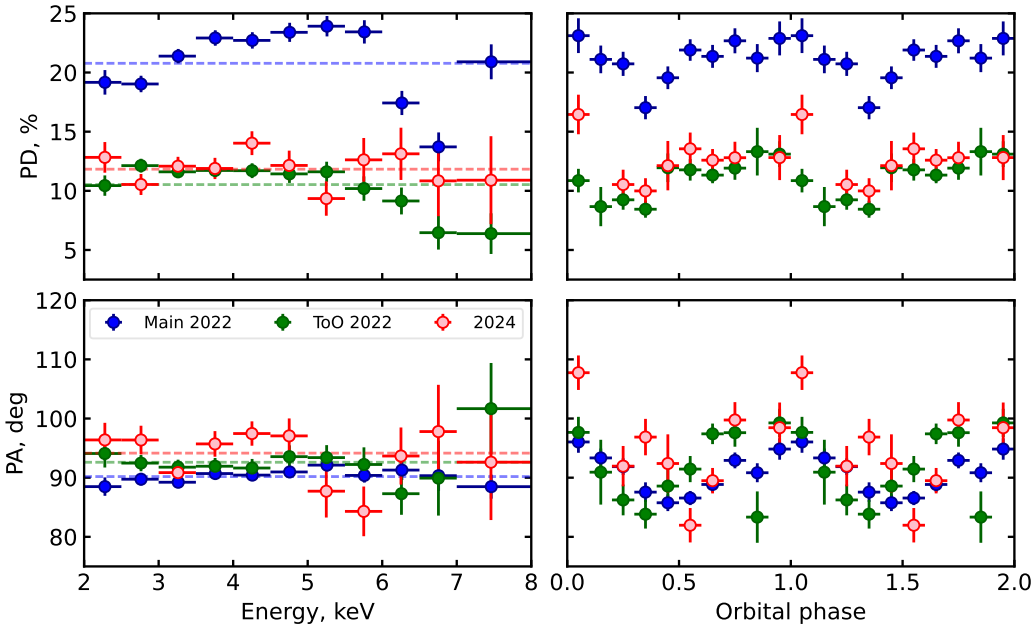

Figure 19. Orbital-phase averaged (*left panel*) and phase-resolved (*right panel*) polarization properties of Cyg X-3 in the hard (**Main 2022**), intermediate (**ToO 2022**) and ultrasoft (**2024**) states observed by *IXPE*. The dashed lines show the parameter averaged across the entire energy band. The figure is created by the author of the thesis.

found to be orthogonal to the position angle of radio ejections and the IR and submillimeter polarization [97–99]. The observed PD (dark blue circles in Fig.19) is constant in the 3.5–6 keV range, but is lower below 3 keV, and in the 6–8 keV range, where the fluorescent and recombination Fe Kα emission lines dominate. The distribution of emitted photons in this process is isotropic, resulting in unpolarized emission. Orbital phase-resolved analysis showed large periodic variations in both PD and PA (see Fig. 19). The pattern is inconsistent with a model of scattering off an optically thin plasma in an orbit with the X-ray source, that was considered in earlier studies [100]. High polarization indicates that the signal is dominated by reflection, with a minor contribution from the intrinsic continuum. Based on this, [44] suggested that the object is obscured by an optically thick medium located high above the orbital plane, shaped like a funnel.

The observation performed during the intermediate state revealed that the PD

in 2–8 keV was reduced by half, to $10.5 \pm 0.3\%$, while the PA remained unchanged at $92.6° \pm 0.8°$. As in the hard state, the PD was lower in the 6–8 keV range due to the presence of an unpolarized iron line emission (green circles in Fig. 19). This indicates that the observed signal is still dominated by reflection, although the funnel parameters have changed. Reduced polarization suggests that reflection and reprocessing might now occur within the surrounding outflow material, rather than just at its surface. This is consistent with the funnel material becoming more transparent.

In the ultrasoft state, the PD was found to be $11.9 \pm 0.5\%$ and the PA was slightly higher than in previous observations, at $94° \pm 1°$, showing no significant energy dependence (pink circles in Fig. 19). The orbital variations of PD are comparable to those observed previously in the hard and intermediate states, while PA shows a prominent peak at phase 0. In contrast to the hard and intermediate states, the iron line is not observed in both spectral and polarimetric properties. Therefore, it is unlikely that the spectrum in the ultrasoft state is dominated by the reflection of a cold, dense medium, as suggested for the hard state in [44].

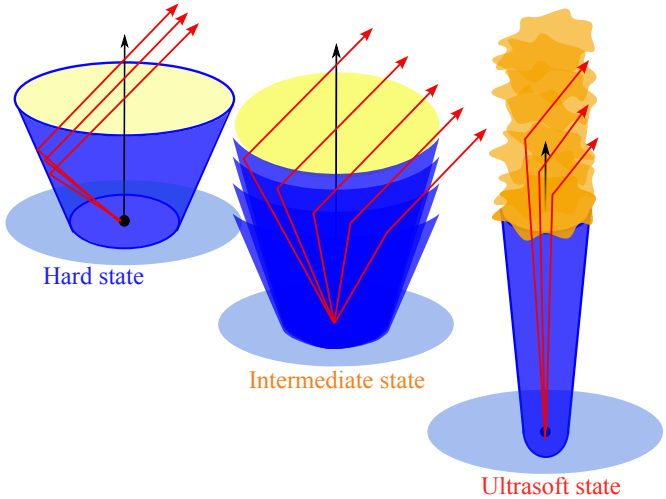

Figure 20. Sketch of the geometry associated with the hard, intermediate, and ultrasoft states. Red arrows indicate direction of the incident and reflected/scattered photons by the optically thick outflow (blue). The figure and description are from [96].

Polarimetric observations of Cyg X-3 across its hard, intermediate, and ultrasoft spectral states enabled the reconstruction of the system's geometry, as illustrated in Fig. 20. In the hard state, the observer sees primarily photons reflected from the back surface of the funnel. In the intermediate state, emission arises from multiple sides of the funnel due to reflection and scattering, as the upper funnel progressively becomes more transparent when the object switches to the soft state. In the soft state, the scattering of radiation by matter along the funnel axis dominates the observed signal, exceeding the reflected component [96].

3.3 Swift J1727.8–1613

Galactic X-ray binary Swift J1727.8–1613 was first detected during its outburst in August 2023 [101], prompting multiwavelength follow-up campaigns by several observatories ([102–107]). Indirect evidence from the multiwavelength spectrum, the presence of QPOs, and optical polarization properties suggest that the binary system contains a black hole. The source is exceptionally bright, during outburst reaching a peak count rate comparable to that of GX 339–4. It is also the first source for which X-ray polarization coverage during a hard-to-soft state transition has been obtained.

IXPE first observed Swift J1727.8–1613 on 2023 September 7 and measured a PD of $4.1\% \pm 0.2\%$ and a PA of $2.2^\circ \pm 1.3^\circ$ [109], which aligns with the optical [110] and submillimeter [111] polarization, and therefore with the jet. After that, *IXPE* made four additional observations of the source, at roughly 10-day intervals, as it transitioned from the hard state to the soft state; these observations are shown in the HID in Fig. 21.

The fourth observation was conducted on 2023 October 4, during which Swift J1727.8–1613 was also observed by *NuSTAR* and *INTEGRAL*. We performed spectral fitting

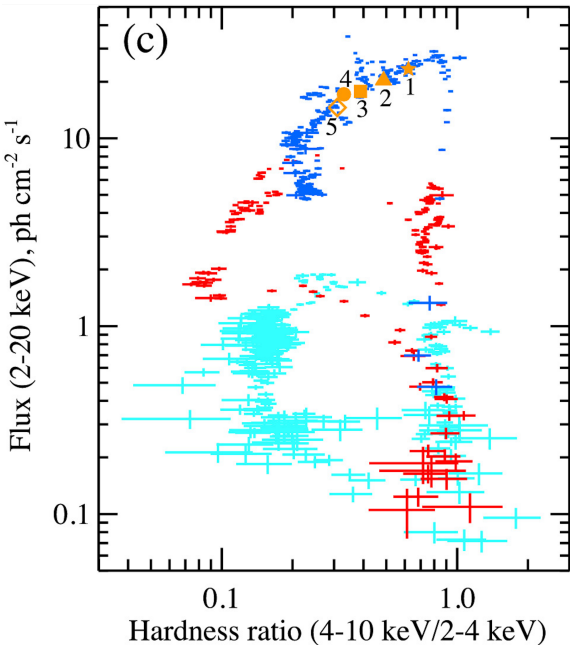

Figure 21. Hardness-intensity diagram: blue crosses show the evolution of Swift J1727.8–1613 during the current outburst. The positions of the source on the diagram during the five *IXPE* observations are shown by the orange symbols. The figure and description are from [108].

analysis of this epoch, using the model

`TBfeo*(diskbb+reflect*compPS)*crabcor`,

combining 6 spectra (two *NuSTAR* detectors, three *IXPE* detectors and one *INTEGRAL* detector) that cover an energy band from 2 to 400 keV. This model combines blackbody emission from the accretion disk [8, 9], hybrid Comptonization [10], and reflection from a neutral medium [112]. The `crabcor` component is a simple power law multiplied by a constant (`Norm` $\times E^{\texttt{dGamma}}$), used for calibration between instruments only and does not contain any physical information. The `Norm` is a free parameter for each spectrum, while `dGamma` is a free parameter for each instrument and links the detectors within one instrument. These two parameters were fixed to 1 and 0 respectively for *INTEGRAL* and the first *NuSTAR* detector. In addition, the `gain` tool in XSPEC was required in *IXPE* detector 3 to avoid calibration problems (shown in Tab. 3).

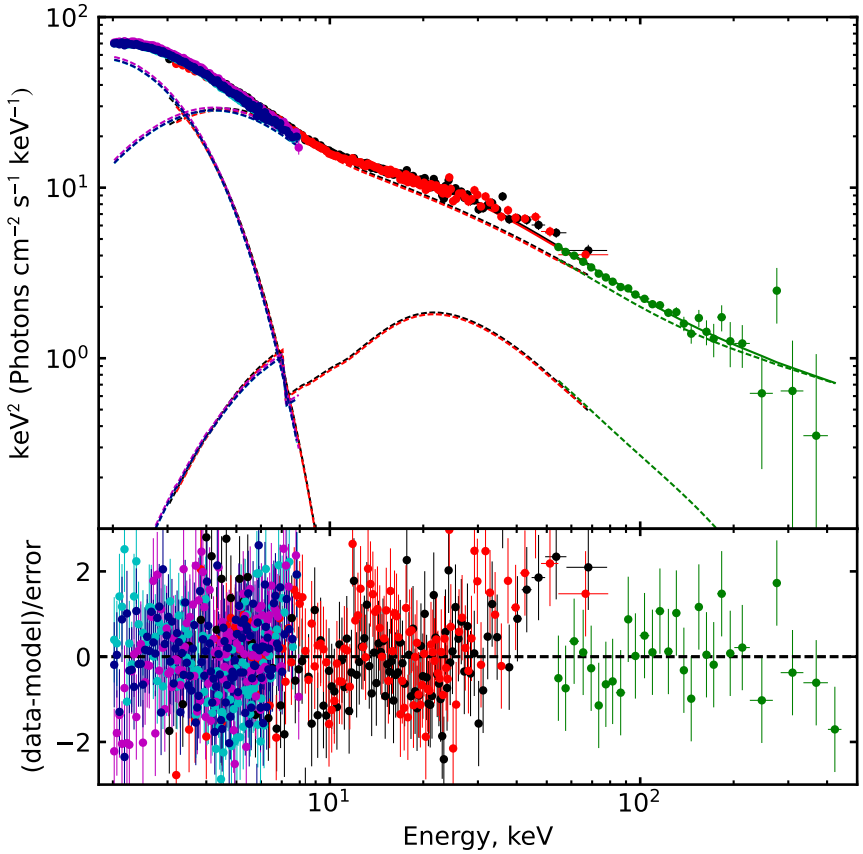

Figure 22. Energy flux spectrum of Swift J1727.8–1613 with the best fit model and components. Three instruments are combined: *IXPE* (cyan, blue, magenta for 3 detectors), *NuSTAR* (black and red for 2 detectors) and *INTEGRAL* (green). The figure is created by the author of the thesis.

The best model parameters are shown in Tab. 2, and the energy flux spectrum with the model is illustrated in Fig. 22. To reduce computational time, the `Gmin` parameter was determined early in the fitting process and frozen at 1.245, the interstellar absorption parameter was fixed since it did not significantly contribute to the chi-square. A systematic error of 0.4% was applied to the data, resulting in fit statistics of $\chi^2 = 1068.19/900$.

We find that the hybrid Comptonization model can adequately describe the spectrum of Swift J1727.8–1613 during its transition toward the soft state. A further improvement to the model would be to reconstruct the polarization properties of

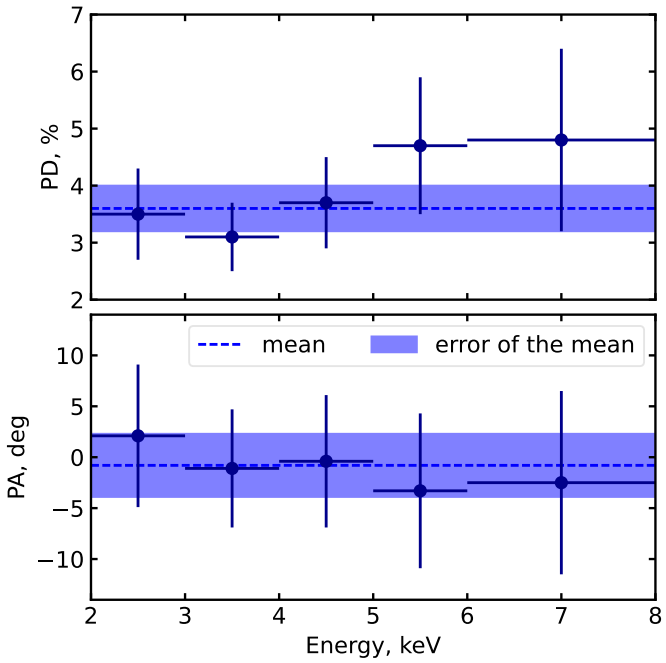

Figure 23. Polarization properties of the fourth *IXPE* observation during Swift J1727.8–1613 hard-to-soft state transition. The figure is created by the author of the thesis.

the corona. Polarimetry measured during the fourth observation is shown in Fig.23. The PD in the 2–8 keV range was $3.6 \pm 0.4\%$, and the PA was $-0.8° \pm 3.1°$. These values were obtained by fitting the *IXPE* data to the simple model with constant polarization `constant*polconst(diskbb+powerlaw)`. The resulting parameters are shown in Tab.4. The `gain` function was used to avoid calibration problems; the parameters are shown in Tab. 5.

To obtain the energy dependence of the polarization, all parameters except polarization were fixed to the previously determined values, and the spectrum was fitted again in the 2–3 keV range, then 3–4 keV, and so on, following the approach described in [108]. The resulting fit statistics is $\chi^2 = 1375.08/1327$. PD was found to increase with energy between 3 and 6 keV, while PA showed no trend. The polarization constraints are consistent with a slab corona and low electron temperature spectrum [10]. Our subsequent work will include direct fitting of broadband spectral and polarimetric data to constrain the parameters of the hot medium.

Table 2. Best fit parameters and values for the broadband spectrum of Swift J1727.8–1613.

No.	Comp	Parameter	Unit	Value
Data group: 1 (NICER det1)				
1	TBfeo	nH	10^{22}	0.291
2	diskbb	Tin	keV	$0.667^{+0.015}_{-0.013}$
2	diskbb	norm	10^4	$4.5^{+0.3}_{-0.4}$
3	reflect	rel_refl		0.32 ± 0.05
5	compPS	kTe	keV	$13.9^{+0.13}_{-0.18}$
5	compPS	EleIndex		$3.21^{+0.12}_{-0.09}$
5	compPS	Gmin		1.245
5	compPS	kTbb	keV	$0.98^{+0.03}_{-0.02}$
5	compPS	tau_y		$1.97^{+0.02}_{-0.06}$
5	compPS	cosIncl		0.89 ± 0.03
5	compPS	norm	10^3	$5.3^{+0.7}_{-0.4}$
Data group: 2 (NICER det2)				
7	crabcor	Norm		0.976 ± 0.003
Data group: 3 (INTEGRAL)				
7	crabcor	dGamma		0.0
7	crabcor	Norm		1.0
Data group: 4 (IXPE det1)				
7	crabcor	dGamma		0.185 ± 0.011
7	crabcor	Norm		1.062 ± 0.018
Data group: 5 (IXPE det2)				
7	crabcor	Norm		1.107 ± 0.019
Data group: 6 (IXPE det3)				
7	crabcor	Norm		1.067 ± 0.018

Table 3. Response parameters of the third *IXPE* detector for the broadband spectrum fit.

Rmodel	**Name**	**Value**
gain	slope	1.0043 ± 0.0014
gain	offset	0.030 ± 0.004

Table 4. Model parameters for *IXPE* polarization fit.

No.	**Model**	**Parameter**	**Unit**	**Value**
Data group: 1 (IXPE det1)				
1	constant	factor		1.0
2	polconst	A		0.036±0.004
3	polconst	psi	deg	-0.8±3.1
4	diskbb	Tin	keV	$0.832^{+0.030}_{-0.018}$
5	diskbb	norm		10200^{+800}_{-4200}
6	powerlaw	PhoIndex		2.2±0.6
7	powerlaw	norm		29^{+59}_{-15}
Data group: 2 (IXPE det2)				
8	constant	factor		1.0368±0.0024
Data group: 3 (IXPE det3)				
15	constant	factor		0.9956±0.0022

Table 5. Response parameters for the *IXPE* polarization fit.

Det.	**Rmodel**	**Name**	**Value**
1	gain	slope	0.984 ± 0.008
1	gain	offset	0.075 ± 0.005
2	gain	slope	0.980 ± 0.008
2	gain	offset	0.049 ± 0.007
3	gain	slope	0.980 ± 0.008
3	gain	offset	0.040 ± 0.006

4 Conclusion and outlook

The results presented in this work demonstrate the potential of X-ray polarimetry for addressing long-standing questions in the physics of X-ray binaries. Polarimetric measurements provide direct insights into the geometry, composition, and physical conditions of the emitting regions in accreting black hole systems, enabling us to probe aspects of their structure that are otherwise inaccessible. By combining polarization with spectral and timing data, we are able to distinguish between emission components and track their evolution across different spectral states.

The future of X-ray polarimetry is especially promising with the upcoming launch of advanced polarimetric observatories, such as the enhanced X-ray Timing and Polarimetry mission (*eXTP*, [113]). Scheduled for launch in the coming years, *eXTP* will combine advanced X-ray timing, spectroscopy, and polarimetry, enabling a comprehensive study of compact objects and their environments with exceptional precision.

In my future work, I will continue refining multi-instrument spectral models for sources such as Swift J1727.8–1613 and Cyg X-1, with a particular focus on incorporating polarimetric data into the modeling framework. I will also pursue further studies of X-ray binaries using X-ray polarimetry, including the analyses of newly discovered transient sources. In addition, I plan to extend my research into the very high energy band by using data from gamma-ray observatories such as *Fermi*-LAT and *H.E.S.S.*, aiming to investigate accreting black holes across the full electromagnetic spectrum.

References

[1] D. Psaltis, Accreting Neutron Stars and Black Holes: A Decade of Discoveries, 2004.

[2] N. I. Shakura and R. A. Sunyaev, Astronomy & Astrophysics **24**, 337–355 (1973).

[3] H.-J. Grimm, M. Gilfanov, and R. Sunyaev, Astronomy & Astrophysics **391**, 923–944 (2002).

[4] A. Avakyan *et al.*, Astronomy & Astrophysics **675**, A199 (2023).

[5] M. Neumann, A. Avakyan, V. Doroshenko, and A. Santangelo, Astronomy & Astrophysics **677**, A134 (2023).

[6] C. Done, M. Gierliński, and A. Kubota, The Astronomy and Astrophysics Review **15**, 1–66 (2007).

[7] M. Gierlinski *et al.*, Monthly Notices of the Royal Astronomical Society **309**, 496–512 (1999).

[8] K. Mitsuda *et al.*, Publications of the Astronomical Society of Japan **36**, 741–759 (1984).

[9] K. Makishima *et al.*, The Astrophysical Journal **308**, 635 (1986).

[10] J. Poutanen and R. Svensson, The Astrophysical Journal **470**, 249 (1996).

[11] A. Ibragimov *et al.*, Monthly Notices of the Royal Astronomical Society **362**, 1435–1450 (2005).

[12] A. A. Zdziarski and M. Gierliński, Progress of Theoretical Physics Supplement **155**, 99–119 (2004).

[13] J. Poutanen, J. Krolik, and F. Ryde, Monthly Notices of the Royal Astronomical Society **292**, L21–L25 (1997).

[14] A. A. Zdziarski, W. N. Johnson, and P. Magdziarz, Monthly Notices of the Royal Astronomical Society **283**, 193–206 (1996).

[15] T. J. Maccarone and P. S. Coppi, Monthly Notices of the Royal Astronomical Society **338**, 189–196 (2003).

[16] R. P. Fender, M. M. Hanson, and G. G. Pooley, Monthly Notices of the Royal Astronomical Society **308**, 473–484 (1999).

[17] S. Markoff, M. A. Nowak, and J. Wilms, The Astrophysical Journal **635**, 1203–1216 (2005).

[18] M. C. Begelman and J. E. Pringle, Monthly Notices of the Royal Astronomical Society **375**, 1070–1076 (2007).

[19] F. Haardt and L. Maraschi, The Astrophysical Journal **380**, L51 (1991).

[20] T. M. Belloni, A. Sanna, and M. Méndez, Monthly Notices of the Royal Astronomical Society **426**, 1701–1709 (2012).

[21] R. A. Remillard and J. E. McClintock, Annual Review of Astronomy and Astrophysics **44**, 49–92 (2006).

[22] T. Belloni, in *The Jet Paradigm* (Springer Berlin Heidelberg , 2009), p. 53–84.

[23] S. Miyamoto *et al.*, The Astrophysical Journal **391**, L21 (1992).

[24] T. M. Belloni and S. E. Motta, in *Astrophysics of Black Holes* (Springer Berlin Heidelberg , 2016), p. 61–97.

[25] T. M. Belloni, S. E. Motta, and T. Muñoz-Darias, Black hole transients, 2011.

[26] P. Uttley and I. M. McHardy, Monthly Notices of the Royal Astronomical Society **323**, L26–L30 (2001).

[27] T. J. Maccarone, P. S. Coppi, and J. Poutanen, The Astrophysical Journal **537**, L107–L110 (2000).

[28] J. Poutanen and A. Veledina, Space Science Reviews **183**, 61–85 (2014).

[29] A. Veledina, J. Poutanen, and I. Vurm, Monthly Notices of the Royal Astronomical Society **430**, 3196–3212 (2013).

[30] S. Miyamoto and S. Kitamoto, Nature **342**, 773–774 (1989).

[31] P. Uttley *et al.*, The Astronomy and Astrophysics Review **22**, (2014).

[32] J. Homan and T. Belloni, Astrophysics and Space Science **300**, 107–117 (2005).

[33] G. G. Stokes, Transactions of the Cambridge Philosophical Society **9**, 399 (1851).

[34] F. Kislat, B. Clark, M. Beilicke, and H. Krawczynski, Astroparticle Physics **68**, 45–51 (2015).

[35] K. C. Westfold, The Astrophysical Journal **130**, 241 (1959).

[36] M. C. Weisskopf *et al.*, The Astrophysical Journal **220**, L117 (1978).

[37] A. M. Bykov, Y. A. Uvarov, P. Slane, and D. C. Ellison, The Astrophysical Journal **899**, 142 (2020).

[38] A. L. Peirson and R. W. Romani, The Astrophysical Journal **885**, 76 (2019).

[39] J. S. Heyl and N. J. Shaviv, Monthly Notices of the Royal Astronomical Society **311**, 555–564 (2000).

[40] R. Taverna *et al.*, Monthly Notices of the Royal Astronomical Society **438**, 1686–1697 (2014).

[41] M. Dovčiak *et al.*, Monthly Notices of the Royal Astronomical Society **391**, 32–38 (2008).

[42] J. D. Schnittman and J. H. Krolik, The Astrophysical Journal **712**, 908–924 (2010).

[43] H. Krawczynski *et al.*, Science **378**, 650–654 (2022).

[44] A. Veledina *et al.*, Nature Astronomy **8**, 1031–1046 (2024).

[45] R. A. Sunyaev and L. G. Titarchuk, Astronomy & Astrophysics **86**, 121 (1980).

[46] A. C. Fabian, M. J. Rees, L. Stella, and N. E. White, Monthly Notices of the Royal Astronomical Society **238**, 729–736 (1989).

[47] P. A. Charles, Black Holes in our Galaxy: Observations, 1998.

[48] J. M. Bardeen, W. H. Press, and S. A. Teukolsky, The Astrophysical Journal **178**, 347 (1972).

[49] M. A. Abramowicz, B. Czerny, J. P. Lasota, and E. Szuszkiewicz, The Astrophysical Journal **332**, 646 (1988).

[50] J. Frank, A. King, and D. Raine, *Accretion Power in Astrophysics* (Cambridge University Press , 2002).

[51] J.-P. Lasota, New Astronomy Reviews **45**, 449–508 (2001).

[52] E. P. T. Liang and R. H. Price, The Astrophysical Journal **218**, 247 (1977).

[53] F. H. Vincent, A. Różańska, A. A. Zdziarski, and J. Madej, Astronomy & Astrophysics **590**, A132 (2016).

[54] D. R. Wilkins and A. C. Fabian, Monthly Notices of the Royal Astronomical Society **424**, 1284–1296 (2012).

[55] M. L. Parker *et al.*, The Astrophysical Journal Letters **821**, L6 (2016).

[56] E. Kara *et al.*, Nature **565**, 198–201 (2019).

[57] C. Bambi, *Black Holes: A Laboratory for Testing Strong Gravity* (Springer Singapore , 2017).

[58] A. M. Beloborodov, The Astrophysical Journal **850**, 141 (2017).

[59] F. Haardt and L. Maraschi, The Astrophysical Journal **413**, 507 (1993).

[60] M. M. Basko and R. A. Sunyaev, Astrophysics and Space Science **23**, 117–158 (1973).

[61] R. R. Ross and A. C. Fabian, Monthly Notices of the Royal Astronomical Society **358**, 211–216 (2005).

[62] C. Bambi *et al.*, Space Science Reviews **217**, (2021).

[63] C. S. Reynolds, Space Science Reviews **183**, 277 (2014).

[64] R. Giacconi, H. Gursky, F. R. Paolini, and B. B. Rossi, Phys. Rev. Lett. **9**, 439 (1962).

[65] W. Forman *et al.*, The Astrophysical Journal Supplement Series **38**, 357 (1978).

[66] A. Santangelo, R. Madonia, and S. Piraino, in *Handbook of X-ray and Gamma-ray Astrophysics* (Springer Nature Singapore , 2023), p. 1–68.

[67] F. A. Harrison *et al.*, The Astrophysical Journal **770**, 103 (2013).

[68] C. Winkler *et al.*, Astronomy & Astrophysics **411**, L1–L6 (2003).

[69] P. Ubertini *et al.*, Astronomy & Astrophysics **411**, L131–L139 (2003).

[70] G. Vedrenne *et al.*, Astronomy & Astrophysics **411**, L63–L70 (2003).

[71] N. Lund *et al.*, Astronomy & Astrophysics **411**, L231–L238 (2003).

[72] J. M. Mas-Hesse *et al.*, Astronomy & Astrophysics **411**, L261–L268 (2003).

[73] M. C. Weisskopf *et al.*, Journal of Astronomical Telescopes, Instruments, and Systems **8**, (2022).

[74] J. E. Davis, The Astrophysical Journal **562**, 575–582 (2001).

[75] P. J. Humphrey, W. Liu, and D. A. Buote, The Astrophysical Journal **693**, 822–829 (2009).

[76] K. A. Arnaud, in *Astronomical Data Analysis Software and Systems V*, Vol. 101 of *ASP Conf. Ser.*, edited by G. H. Jacoby and J. Barnes (Astron. Soc. Pac. San Francisco, 1996), pp. 17–20.

[77] R. Bellazzini *et al.*, in *Space Telescopes and Instrumentation II: Ultraviolet to Gamma Ray*, edited by M. J. L. Turner and G. Hasinger (SPIE , 2006), Vol. 6266, p. 62662T.

[78] P. Soffitta *et al.*, The Astronomical Journal **162**, 208 (2021).

[79] L. Baldini *et al.*, SoftwareX **19**, 101194 (2022).

[80] S. Bowyer, E. T. Byram, T. A. Chubb, and H. Friedman, Science **147**, 394–398 (1965).

[81] J. C. A. Miller-Jones *et al.*, Science **371**, 1046–1049 (2021).

[82] L. Gou *et al.*, The Astrophysical Journal **790**, 29 (2014).

[83] A. M. Stirling *et al.*, Monthly Notices of the Royal Astronomical Society **327**, 1273–1278 (2001).

[84] M. C. Weisskopf *et al.*, The Astrophysical Journal **215**, L65 (1977).

[85] P. Laurent *et al.*, Science **332**, 438–439 (2011).

[86] M. Chauvin *et al.*, Nature Astronomy **2**, 652–655 (2018).

[87] V. Kravtsov *et al.*, Variability of X-ray polarization of Cyg X-1, 2025.

[88] R. Giacconi, P. Gorenstein, H. Gursky, and J. R. Waters, The Astrophysical Journal **148**, L119 (1967).

[89] P. C. Gregory *et al.*, Nature **239**, 440–443 (1972).

[90] W. B. Atwood *et al.*, The Astrophysical Journal **697**, 1071–1102 (2009).

[91] M. L. McCollough, L. Corrales, and M. M. Dunham, The Astrophysical Journal **830**, L36 (2016).

[92] I. I. Antokhin and A. M. Cherepashchuk, The Astrophysical Journal **871**, 244 (2019).

[93] I. I. Antokhin, A. M. Cherepashchuk, E. A. Antokhina, and A. M. Tatarnikov, The Astrophysical Journal **926**, 123 (2022).

[94] A. Szostek, A. A. Zdziarski, and M. L. McCollough, Monthly Notices of the Royal Astronomical Society **388**, 1001–1010 (2008).

[95] A. A. Zdziarski, A. Segreto, and G. G. Pooley, Monthly Notices of the Royal Astronomical Society **456**, 775–789 (2016).

[96] A. Veledina *et al.*, Astronomy & Astrophysics **688**, L27 (2024).

[97] J. Martí, J. M. Paredes, and M. Peracaula, The Astrophysical Journal **545**, 939 (2000).

[98] J. C. A. Miller-Jones *et al.*, The Astrophysical Journal **600**, 368 (2004).

[99] T. J. Jones *et al.*, Astronomical Journa **108**, 605 (1994).

[100] J. C. Brown, I. S. McLean, and A. G. Emslie, Astronomy & Astrophysics **68**, 415 (1978).

[101] J. A. Kennea and Swift Team, GRB Coordinates Network **34540**, 1 (2023).

[102] H. Negoro *et al.*, GRB Coordinates Network **34544**, 1 (2023).

[103] M. C. Baglio *et al.*, The Astronomer's Telegram **16225**, 1 (2023).

[104] Y. D. Wang and E. C. Bellm, The Astronomer's Telegram **16209**, 1 (2023).

[105] D. Williams-Baldwin *et al.*, The Astronomer's Telegram **16231**, 1 (2023).

[106] J. C. A. Miller-Jones *et al.*, The Astronomer's Telegram **16271**, 1 (2023).

[107] B. O'Connor *et al.*, The Astronomer's Telegram **16207**, 1 (2023).

[108] A. Ingram *et al.*, The Astrophysical Journal **968**, 76 (2024).

[109] A. Veledina *et al.*, The Astrophysical Journal Letters **958**, L16 (2023).

[110] V. Kravtsov *et al.*, The Astronomer's Telegram **16245**, 1 (2023).

[111] S. D. Vrtilek, M. Gurwell, M. McCollough, and R. Rao, The Astronomer's Telegram **16230**, 1 (2023).

[112] P. Magdziarz and A. A. Zdziarski, Monthly Notices of the Royal Astronomical Society **273**, 837–848 (1995).

[113] A. D. Rosa *et al.*, Science China Physics, Mechanics & Astronomy **62**, (2018).

This thesis was created with the help of AI-based writing tools, including ChatGPT. AI was used to refine the structure, improve clarity and coherence, while all research ideas, methodologies, and content are the original work.